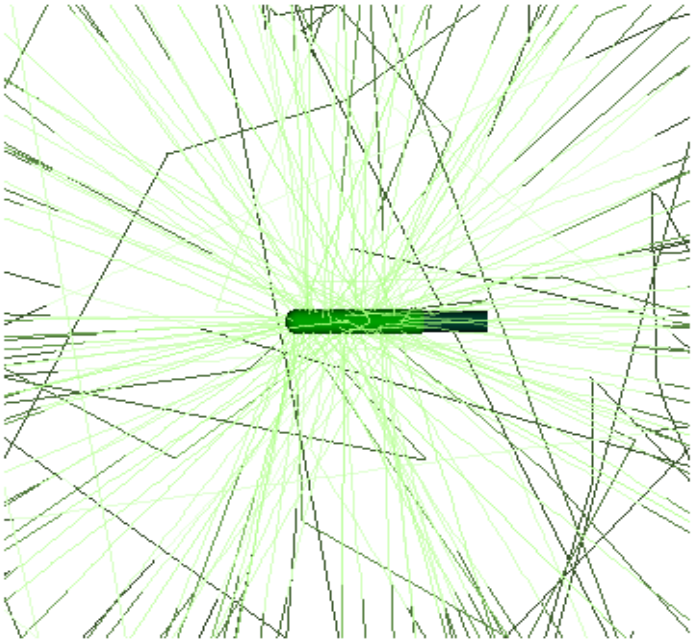

Monte Carlo simulations for brachytherapy

From characterization of a high-dose-rate source to comparison of dose distributions

Master's thesis in Complex Adaptive Systems

MIRIAM SKARIN

DEPARTMENT OF MATHEMATICAL SCIENCES

CHALMERS UNIVERSITY OF TECHNOLOGY
Gothenburg, Sweden 2021
www.chalmers.se

Master's thesis 2021

Monte Carlo simulations for brachytherapy

From characterization of a high-dose-rate source to comparison of dose distributions

MIRIAM SKARIN

CHALMERS
UNIVERSITY OF TECHNOLOGY

Department of Mathematical Science
Division of Applied Mathematics and Statistics
Chalmers University of Technology
Gothenburg, Sweden 2021

Monte Carlo simulations for brachytherapy
From characterization of a high-dose-rate source to comparison of dose distributions
MIRIAM SKARIN

© MIRIAM SKARIN, 2021.

Supervisors: Erik Engwall and Tom Niessen, RaySearch Laboratories AB
Examiner: Torbjörn Lundh, Department of Mathematical Sciences

Master's Thesis 2021
Department of Mathematical Sciences
Division of Applied Mathematics and Statistics
Chalmers University of Technology
SE-412 96 Gothenburg
Telephone +46 31 772 1000

Cover: Particle tracks from a radiating brachytherapy source constructed with Monte Carlo simulations in egs_brachy. Each line corresponds to a travelling particle.

Typeset in LaTeX
Gothenburg, Sweden 2021

Monte Carlo simulations for brachytherapy
From characterization of a high-dose-rate source to comparison of dose distributions
MIRIAM SKARIN
Department of Mathematical Sciences
Chalmers University of Technology

Abstract

Brachytherapy is an internal radiation treatment where a small, encapsulated radioactive source is placed at different dwell positions close to or within the tumor. The standard method for treatment planning in brachytherapy is to follow the TG43-formalism where the full patient geometry is treated as water. This approximation has limitations in the modelling of skin–air interfaces and tissue variations and does not take into consideration shielding effects. To overcome the limitations of this analytical framework, Monte Carlo (MC) simulations can be used. To reduce the computational time, which is often a limiting factor in MC computations, pre-generated information about the radiation can be utilized. In this work, independent Monte Carlo simulations performed with the software egs_brachy are setup to characterize the radiation from a high-dose-rate brachytherapy source. The output is a phase space with information about the radiation properties. The phase space is analyzed and resulted in a 4D-histogram which can be used as an input to the brachy Monte Carlo dose engine prototype in the treatment planning system RayStation®. In addition to constructing the input data, dose distributions for two different treatment plans are scored with egs_brachy in both water and tissue. The same treatment plans are used to compute dose with TG43 and the brachy Monte Carlo prototype and the dose distributions are compared with the ones obtained with egs_brachy. Local gamma tests were performed with gamma criteria (1%/1 mm) and (3%/2 mm), yielding low fail rates in comparison to both RayStation dose engines. The favorable gamma results show that both TG43 and the brachy Monte Carlo dose engine can reproduce the simulated dose distributions from egs_brachy well. In conclusion, the produced phase space is suitable as input for the brachy MC dose engine and the simulated dose distributions can be utilized in a validation framework.

Keywords: brachytherapy, treatment planning, dose calculation, Monte Carlo simulations, phase space

Acknowledgements

First of all, I would like to thank RaySearch Laboratories for giving me this great opportunity to combine my biggest interests when doing my master's thesis. I would also like to express my sincere gratitude to my supervisors Erik Engwall and Tom Niessen, for all your input and enthusiasm in this project. From the shortest meetings to the longest discussions have you been encouraging and helpful, always teaching me new things. Thanks also for all the small chats and side tracks, now I know more about ice-skating than ever before.

I also want to thank all members of the Brachy team for warmly welcoming me into your fantastic group. This spring would never have been the same without you! Thanks also to Torbjörn Lundh at Chalmers for taking time to examine this project and answering all my questions.

Last but not least, I would like to thank Norea. Thank you for all your pep-talks, discussions and support during this thesis work (and the entire education!). I cannot imagine a better friend to get through those amazing five years with.

Miriam Skarin, Gothenburg, June 2021

Contents

List of Abbreviations **xi**

1 Introduction **1**
1.1 Background . . . 1
1.2 Scope . . . 3
1.3 Thesis outline . . . 4

2 Theory **5**
2.1 Radiation therapy . . . 5
2.2 Brachytherapy as cancer treatment . . . 5
2.3 Particle transportation in matter . . . 6
2.3.1 Photon interactions with media . . . 8
2.3.2 Electron interactions with media . . . 8
2.4 Monte Carlo simulations of particle transport . . . 9
2.4.1 Generating random numbers . . . 9
2.4.2 Sampling of physical processes . . . 10
2.4.3 The software EGSnrc and egs_brachy . . . 12

3 Methodology **17**
3.1 Software setup . . . 17
3.2 The source microSelectron-v2 . . . 17
3.3 Design of input data for a brachy Monte Carlo dose engine . . . 18
3.3.1 Scoring of phase space with egs_brachy . . . 18
3.3.2 Introduction of new coordinates . . . 20
3.4 Comparison of dose distributions . . . 22
3.4.1 Determination of dwell positions and dwell times in egs_brachy 22
3.4.2 Scoring of dose distributions with egs_brachy . . . 23
3.4.3 Methods for comparison of dose distributions . . . 24

4 Results and Discussion **27**
4.1 Phase space analysis . . . 27
4.2 Comparison of dose distributions calculated with RayStation® and egs_brachy . . . 33
4.2.1 Head-and-neck case . . . 33
4.2.2 Breast case . . . 36

5 Conclusions **41**

5.1 Future work 41

Bibliography **43**

List of Abbreviations

AAPM-TG43	Association of American Physicists in Medicine TaskGroup No.43
BMC	Brachy Monte Carlo dose engine
CDF	Cumulative distribution function
CT	Computed tomography
DICOM	Digital Imaging and Communications in Medicine
DTA	Distance to agreement
EBRT	External beam radiation therapy
HDR	High dose rate
MBDCA	Model based dose calculation algorithm
MC	Monte Carlo
OAR	Organs-at-risk
RNG	Random number generator
RTPlan	Radiotherapy plan. Tag used in DICOM
TPS	Treatment planning system

1 | Introduction

1.1 Background

Each year about 65 000 people are diagnosed with cancer in Sweden. This is a life-changing disease for the patients and the people around them. Today, the three biggest techniques to treat cancer are surgery, chemotherapy and radiation therapy [1]. The latter includes both external beam radiation therapy (EBRT) and internal radiation therapy, also known as *brachytherapy*. In EBRT, the treatment is carried out by delivering high-energy radiation to the target from different directions, i.e. beams, from outside the patient. Brachytherapy instead uses a small, radioactive source placed inside the patient. By placing it at different positions close to or within the tumor, the deposited dose is high and localized which in turn reduces the damage to surrounding normal tissue [2].

A treatment planning system (TPS) is a software package, which is used to determine a suitable radiation treatment plan for a patient. RaySearch Laboratories AB is a software company within medical science, which develops and provides the treatment planning system RayStation®. This is a world-leading TPS within external beam radiotherapy, where the radiation source instead originates from an accelerator outside the patient. To fulfill the vision to be able to plan for all types of radiation treatments within RayStation®, RaySearch just recently entered the field of brachytherapy.

For brachytherapy the standard method for calculating the deposited dose is to follow the Association of American Physicists in Medicine Task Group No.43 formalism (AAPM-TG43), often written as TG43. It has been implemented in many brachytherapy TPSs and is also the method implemented in the brachytherapy dose engine in RayStation®. TG43 is an analytical framework where the full patient geometry is treated as water. The concept and theory [3], [4], as well as the limitations [5], [6], [2] of this framework are described in detail in the literature. In short, the TG43 dose engine reports absorbed dose at a point using an analytical model with parameters tabulated for each source type used [6]. The tabulated data is obtained through measurements or Monte Carlo simulations in an unbounded spherical water phantom. By superposition of single-source dose distributions, the full dose distribution from a complete treatment plan may then be obtained. The main approximation done is treating the full patient geometry as water. For many brachytherapy treatments this is a valid approximation, but there are also cases

where it is not. Several studies have shown that the dose distribution is inaccurately modelled for treatment sites such as the cervical area [7], skin [8] and breast [9], among others. To approximate the full patient geometry with water has the following implications:

- Full scatter conditions cannot be properly modelled for superficial treatment sites. The volume outside the patient is also seen as water by the TG43 dose engine. Therefore, TG43 assumes that particles are being scattered into the patient to a higher extent than in reality, leading to an overestimated dose. This includes cases as breast and head-and-neck.
- Tissue variations are not considered. This will have higher influence for tissue where the density compared with water differ (e.g. bones) or sites close to air cavities (e.g the lungs) [10].
- Shielding effects are not considered. Metal shielding can be used to reduce dose to organs-at-risk (OAR). Neglecting this effect will overestimate dose to OARs which is in the right direction with respect to clinical impact, but on the other hand, reduce the dose to the tumor [11].

Due to the limitations of TG43, the use of model-based dose calculation algorithms (MBDCAs) will be important to advance brachytherapy treatment planning [12]. MBDCAs such as the collapsed-cone superposition/convolution algorithm [13], grid-based Boltzmann equation solver [14] and the Monte Carlo (MC) method, have the ability to model the dose distribution more accurately than TG43. Figure 1.1 shows an example of dose difference between a dose distribution computed by the Monte Carlo-code egs_brachy and dose computed with the TG43-formalism for the same breast case. The eight circles are the channels where the radioactive source is inserted during the treatment. The dose difference is calculated as D_{egs} - D_{TG43} with D_x being the dose calculated with the engine x. The darker blue parts shows that TG43 estimates a higher dose than the MC, e.g. close to the skin–air interface. This is due that TG43 is based on full scatter conditions with water outside the patient volume.

In radiotherapy, Monte Carlo (MC) computations are considered state-of-the-art to achieve high accuracy [2]. The method is based on the law of big numbers and the central limit theorem [2]. By sampling random numbers according to a certain distribution, a model of a behaviour can be obtained. MC simulations can be time consuming and in order to save time when applying this technique in treatment planning for brachytherapy, pre-simulated information about the properties of the particles when exiting the source surface can be used. This includes the type, energy, direction, and their location on the source. A *phase space* data file compiles this information and may serve as the starting point for the transport of the particles from the source through the patient. The phase space file can be derived using an external MC code, which often results in large file sizes due to each particle being explicitly described [2]. To reduce the file size for inclusion in a TPS, particles with common properties can be grouped together in a histogram, forming a reduced phase space. The particles could then be sampled from the reduced phase space or from a

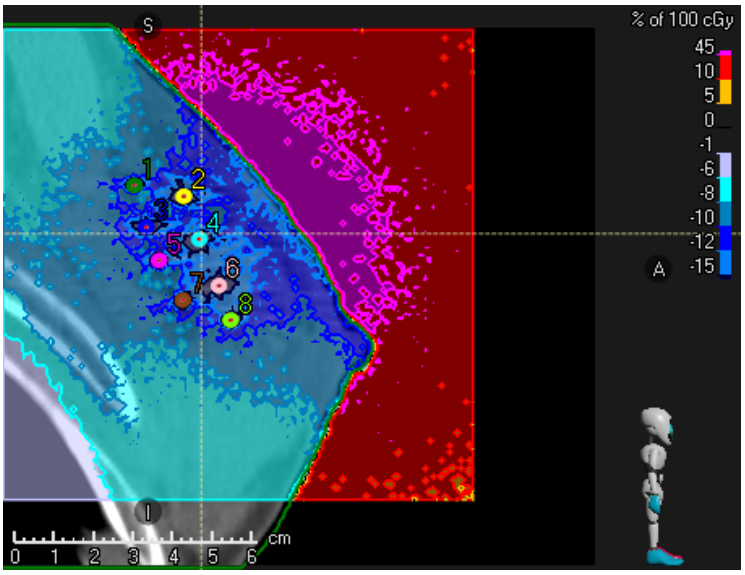

Figure 1.1: Difference plot of the two dose distributions calculated by the Monte Carlo-code egs_brachy and TG43. The difference is defined as D_{egs} - D_{TG43}. TG43 estimates a higher dose than the MC, e.g, close to the skin-air interface.

parameterization of it, rather than from the original large file.

1.2 Scope

The scope of this thesis is to produce and analyze input data for a Monte Carlo dose engine for brachytherapy at the company RaySearch Laboratories AB. Additionally, the project will result in material to be used for the validation of the brachy Monte Carlo dose engine and the today used TG43 dose engine. This can be summarized in the following objectives:

- To set up independent Monte Carlo simulations to characterize a clinically used brachytherapy source by its physical properties.
- To design a reduced phase space from the characterization for inclusion in the internal brachy Monte Carlo dose engine prototype.
- To set up independent Monte Carlo simulations to extract dose distributions in a water phantom from a brachytherapy source for comparison with the existing TG43 dose engine.
- To set up independent Monte Carlo simulations to extract dose distributions in patient phantoms from a brachytherapy source for validation of the brachy Monte Carlo dose engine.

The main limitations of the thesis are described in the following paragraphs.

Monte Carlo simulation tool

The simulation tool used in this study is egs_brachy. This is based on the software tool Electron Gamma Shower nrc (EGSnrc), made to perform Monte Carlo simulation of ionizing radiation transport through matter. Other Monte Carlo simulation tools are not considered due to the availability and strengths of the egs_brachy tool.

Type of brachytherapy

One way of classifying brachytherapy treatment is according to the radiation rate. There is low-dose-rate (LDR), high-dose-rate (HDR) or pulsed-dose-rate (PDR) brachytherapy. The thesis will only be focused on HDR treatment and thus refer to this class when describing brachytherapy.

Brachytherapy source

In this thesis the focus will be on one high energy source of the isotope ^{192}Ir, excluding other types. More specific, the microSelectron-v2 (HDR) source from Elekta (Stockholm, Sweden) will be considered. This source was selected since it was predefined within the simulation tool and also had an easy geometry.

1.3 Thesis outline

The thesis is structured as follows. Chapter 1 has introduced the background and aim of the project. In Chapter 2, the reader may take part of the project's theoretical framework including a description of the software egs_brachy and brachytherapy treatment. The methodology is then presented in Chapter 3. This chapter is divided in two parts: first the phase space analysis, including simulation of raw data and introduction of new coordinates to form the reduced phase space. This is followed by the framework for comparison of dose distributions. In Chapter 4, the results are presented and discussed. Lastly, in Chapter 5, some final conclusions are made to summarize the thesis and what future work that could be done.

2 | Theory

2.1 Radiation therapy

Since the end of the 19th century, the use of ionizing radiation has played a big role in cancer treatment. Shortly after Röentgen discovered X-rays in 1895 and Marie and Pierre Curie discovered radium 1898, the use of external radiation therapy and internal radiation therapy, respectively, begun [15], [16]. Radiation therapy can be delivered both as external beam radiation therapy (EBRT), where the radiation originates from outside of the patient, and internal radiation therapy, such as brachytherapy. When the radiation hits the target the atoms or molecules of the traversed tissue becomes ionized by absorbing or emitting electrons. These ions may then react with surrounding tissue and harm the DNA of the cells. This phenomenon is what radiation therapy takes advantage from; by damaging the DNA of the cancer cells the patient may be cured [17]. The drawback is that the DNA of adjacent healthy tissue often gets damaged as well. These cells are though more likely to recover, while the cancer cells have less capacity of repairing [18].

A tumor is localized with some imaging technique such as computed tomography (CT) or magnetic resonance. This information is then imported to the TPS to make a treatment plan. One technique used is inverse planning, where the therapist can decide on the desired dose levels to certain organs/volumes and the TPS calculates a good plan for the treatment by fulfilling these requirements. This is achieved through mathematical optimization. An approved treatment plan is then the one describing the radiation procedure. This is saved in the format DICOM-RT as an RTPlan.

2.2 Brachytherapy as cancer treatment

Brachytherapy is an internal radiation treatment technique. It uses a radioactive source which can be inserted through special applicators in cavities (intracavitary) or directly in the tissue through needles (interstitial). The source could also be placed directly on the surface of the skin. The term *brachy* means "short" in Greek and the name gives a good clue of the source's location with respect to the tumor. An advantage of using this treatment is the high dose given to a small and well-defined treatment volume, with small effects to surrounding tissue. It is commonly used to treat cancers of the cervix, prostate, breast, and skin [19].

When brachytherapy was first introduced, the radioactive sources were implanted manually by medical personnel, exposing them to harmful radiation. Since the end of last century there are instead remote afterloaders which move the source to given locations inside applicators placed close to or at the tumor. These applicators consist of catheters in the case of intracavitary brachytherapy or needles in the case of interstitial treatment. They are commonly mentioned as channels, inside which the source is stepped through with help of an attached cable at one end. This stepping is performed between different *dwell positions* and the time at a certain position is the *dwell time*. The dwell positions and the dwell times are determined during the treatment planning when a treatment plan is set up. A treatment plan may have several dwell positions, distributed over many channels. When the source has stepped through all positions in one channel, it is retracted to a shielded safe inside the afterloader via transfer tubes, and then transferred to the next channel. The shielded safe is made of tungsten or depleted uranium and is the location of the source when it is not in treatment mode. The needles have diameters from 1.27 mm going up to 1.5 mm [2] and the source moves inside the channels with a speed between 300 to 630 mm/s, recorded for the different makes on the market.

A treatment can be classified with respect to the treatment time (temporary or permanent) but also with respect to the dose rate of the source. High dose rate (HDR) is when the source deliver more than 12 Gy/h and low dose rate (LDR) when it delivers 0.4–2 Gy/h [20]. The most commonly used isotope for HDR is the photon-emitting Iridium-192 (^{192}Ir) with a half-life of 73.83 days. Other isotopes ised for HDR-sources are Cs-137 and Co-60 [2], [16].

It is not only the location of the radiating source that distinguish brachytherapy from other radiation treatments. Something else is the radiation energy. For EBRT with X-rays (photons) the energy often is between 4-18 MeV, while a high energy for brachytherapy is if the source has a mean energy around 0.3 MeV. This leads to short ranging radiation. The mean free path for photons with energy 2 MeV is around 29 cm, while for 100 keV photons it is instead around 7 cm. Ranges in brachytherapy are thus small. The low energies are also one of the reasons why the water approximation, described in the background section, works for many cases in brachytherapy.

2.3 Particle transportation in matter

When high energy particles travel in space, they will interact with other particles and atoms[1]. One example is the production of ions as described in the chapter of radiation therapy. The properties of the particle, e.g. the type, charge and energy, and the atomic composition of the target will affect which interactions that will take place and how much energy will be deposited.

The probability for a specific interaction i is given by the cross section for the

[1] If the space is non-vacuuum.

current medium, usually denoted σ_i. This, together with the medium specifications, form the interaction probability per unit path length

$$\mu_i = \frac{\rho N_A}{\mathrm{M}}\sigma_i \quad [\mathrm{cm}] \tag{2.1}$$

where ρ is the density of the target medium, N_A is the Avogadro constant and M the molar mass of the target [21]. In the case of photons this is called the linear attenuation coefficient for an interaction i. The total interaction probability for the particle can be obtained by adding the probability for all n possible interactions according to

$$\mu \equiv \mu_{tot} = \mu_1 + \mu_2 + ... + \mu_n. \tag{2.2}$$

The path length s that a particle travels from its current position to the site of the next interaction is a random quantity. The probability density function $p(s)$ of the path length s is given by the attenuation law

$$p(s)ds = \mu e^{-\mu s} ds \tag{2.3}$$

and the mean free path λ to next interactions is then

$$\lambda \equiv < s >= \int_0^\infty sp(s)ds = \mu \int_0^\infty se^{-\mu s} ds = \frac{1}{\mu}. \tag{2.4}$$

This is valid under the assumption that the particle travels in homogeneous media [12]. In the case of non-homogeneous media, the mean free path is instead obtained by summing over the path fractions s_j until the interaction point P:

$$\lambda = \sum_{start}^{P} \frac{s_j}{\mu_j}. \tag{2.5}$$

Figure 2.1 shows the path of a particle traveling in two different materials. At each interaction, marked with A and B in the figure, it gets a new direction $\hat{v}$ and energy E. The two paths s_{P1} and s_{P2} will be summed as in Equation 2.5 to obtain the mean free path until the final point P.

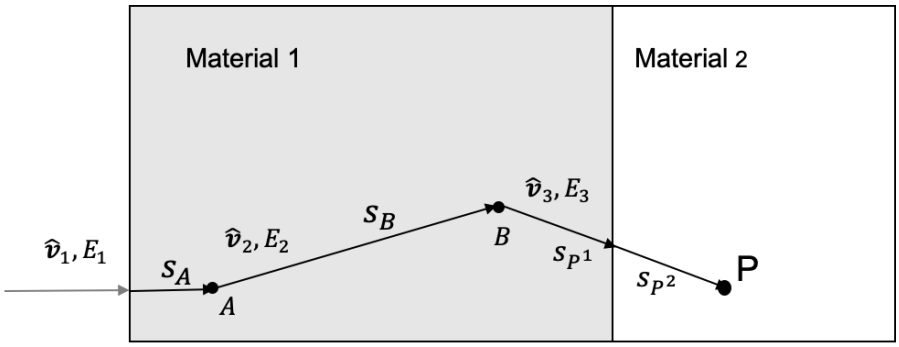

Figure 2.1: Illustration of path length s_A and s_B the particle travels before an interaction of type A and type B occurs respectively. The particle gets a new direction and energy after each interaction. When traveling in two different materials the two paths s_{P1} and s_{P2} are obtained in their respective material.

2.3.1 Photon interactions with media

Photons interact with matter mainly by four different processes: photoelectric absorption, Rayleigh scattering, Compton scattering and pair production [20]. These four processes will be described in the following sections.

Photoelectric absorption Also called the photoelectric effect. A photon with energy E interacts with an inner shell electron with binding energy U_i in an atom. The so called photoelectron is ejected from the shell with the energy E- U_i and the photon is absorbed. The now unstable atom fills the inner shell vacancy with an electron from a higher energy state. This transition leads to emission of energy in form of fluorescent photons and Auger electrons [20].

This process is predominant for photons with relatively low energies and matter with high atomic number Z. The cross-section is approximately proportional to something as

$$\sigma_{pe} \propto \frac{Z^n}{E^3} \tag{2.6}$$

where the exponent n varies between 3 and 4 depending on the photon energy.

Rayleigh Scattering Also called coherent scattering. The incoming photon scatters from atoms, molecules or other structures in the material without any significant energy loss. The scattering is elastic and only changes the direction of the photon. The interaction is common for low energy photons.

Compton Scattering Also called incoherent scattering. Most common at energies in order of 1 MeV. The photon scatters against an atomic electron which is set in motion. The atom fills the vacancy in the same manner as in the photo electric effect and energy is emitted. In contrast to photoelectric absorption, the photon is not actually absorbed but loses energy, i.e. compton shift.

Pair Production The incoming photon interacts with an atom and gets absorbed, producing an electron-positron pair. This interaction has an energy threshold of 1.022 MeV due to the electron rest energy at 511 keV. The probability for pair production to occur increases rapidly with photon energies higher than the threshold but is zero otherwise.

2.3.2 Electron interactions with media

Electrons are constantly losing energy when traveling in media due to inelastic scattering and radiation [22]. The inelastic scattering occurs from atomic electrons which results in ionization and excitation of the atoms. This leads to emission of electrons and photons when the excited atom relaxes. Radiative energy loss occurs via the bremsstrahlung process. The incoming electron interacts with the electromagnetic field of a nucleus and produces a bremsstrahlung photon. This process is dominant for electron energy loss at high energies while the inelastic scattering is

more important to consider at low electron energies. Electrons are also frequently interacting via elastic scattering from atomic nuclei which conserves their energy but changes the path [23].

2.4 Monte Carlo simulations of particle transport

Modelling radiation transport is a complex problem. Attenuation and scattering of photons with secondary particles and resulting new interactions need to be handled. To achieve a good model of the coupled system of transport equations, the Monte Carlo (MC) technique can be used. This method uses sampling of random numbers to calculate integrals or to solve equations, such as the system of coupled transport equations just mentioned. Monte Carlo simulations are applied in a variety of areas and are a good resource in radiation transport to simulate the trajectories of the particle and the type of interaction taking place. The steps to perform particle transport in media with the use of MC can be summarized as follows:

1. The current particle's properties (type, energy, position and direction) are sampled from respective distribution.
2. The distance to the next interaction point X is determined from the total cross section.
3. The particle is transported to interaction point X.
4. If the particle still is within the geometry of interest, determine which process that occurs.
5. The properties of the resulting particle(s) are sampled.
6. Start from step 2 again. Repeat until the current particle leaves the geometry of interest or reaches the lower transport threshold.

These steps are then performed for the resulting particles until no primary nor secondary particles are left [23]. This can also be visualized in a scheme as in Figure 2.2. One initial particle generated is said to be one *history*. Quantities of interest, as absorbed dose in the case of dosimetry, can be calculated by averaging over all simulated particle histories N. By the central limit theorem, MC estimates of quantities is subject to a statistical uncertainty $\propto 1/\sqrt{N}$.

2.4.1 Generating random numbers

Briefly, the basic principle of an MC simulation is sampling of random numbers from a certain distribution. This requires a high-quality random number generator (RNG), which can perform sequences long enough to make numbers be considered "random" [12]. Within radiation therapy, long-sequence RNGs are necessary. One example is the RANMAR from the CERN library (http://www.cern.ch). Another example of a more simple RNG is

$$I_{j+1} = aI_j + b \pmod{c} \tag{2.7}$$

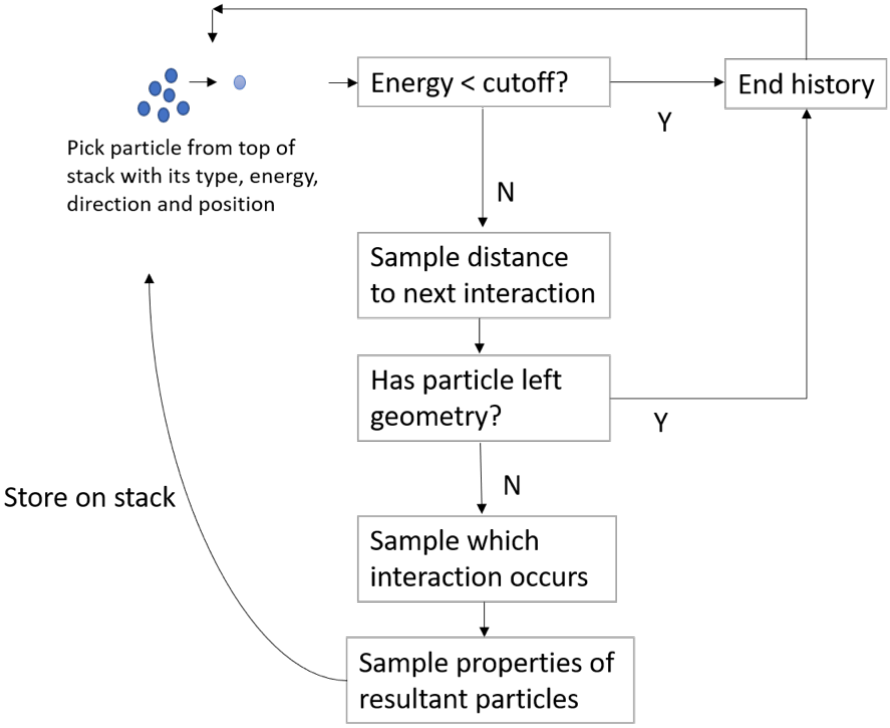

Figure 2.2: A scheme over particle transport with help of MC simulations.

where a and b are integers and c the value to take modulus with, i.e the remainder when the integer $(aI_j + b)$ is divided by c. The value I_0 is set to a given start value. This produces integers between 0 and c-1 and the uniform random number $r \in [0, 1)$ is then obtained by

$$r_i = \frac{I_i}{c}. \tag{2.8}$$

2.4.2 Sampling of physical processes

In the case of radiation transport, the physical processes and particle properties are described by probability distributions determined by the cross section σ. The majority of them are not following a uniform distribution. To sample random numbers within the range $[a, b]$ from a probability function $p(x)$, the cumulative distribution function CDF $P(x)$ is used. This is given by

$$P(x) = \int_a^x p(x')dx', \; a \leq x \leq b \tag{2.9}$$

with $P(a) = 0$ and $P(b) = 1$. A random number $r \in [0, 1]$ is sampled and the value x' can be obtained from the distribution according to

$$r = P(x') = \int_a^{x'} p(x)dx \tag{2.10}$$

by calculating

$$x' = P^{-1}(r). \tag{2.11}$$

This method is called the *transformation* method and is visualized in Figure 2.3 with use of a normal distribution. The method depends on the existence of the inverse of $P(x)$ [12]. The distance l to next interaction point X for an particle is one example of a quantity sampled from a continuous PDF. The value is given by integration and inversion of the PDF in Equation 2.3:

$$l = -\lambda \log r, \tag{2.12}$$

where r is an unitary random number and λ the mean free path.

In the discrete case, such as sampling of which interaction that occurs, the corresponding probability density function is denoted probability mass function, p_i, where p_i is the probability that the outcome is the interaction with index i. The values p_i have to be non-negative and fulfill

$$\sum_{i=1}^{n} p_i = 1, \tag{2.13}$$

where n represents the number of possible interactions. The corresponding CDF for interaction i is given by

$$P_i = \sum_{j=1}^{i} p_j. \tag{2.14}$$

To choose among two interactions with correct probabilities using a unitary random number r, interaction 1 is chosen if $r < p_1$ and interaction 2 is chosen otherwise. When having n possible interactions to choose among, the interaction is determined by the value of i, fulfilling the condition

$$P_{i-1} \leq r \leq P_i, \quad i = 1, 2...n \tag{2.15}$$

with $P_0 = 0$. The discrete CDF with $p_i = \mu_{x_i}/\mu_{tot}$, where μ_{tot} is the sum of all n possible interactions, is used to sample which interaction x_i with probability p_i to occur at an interaction point.

There are other methods to obtain x', like the rejection method, but they will not be described here. The interested reader can refer to references [24] and [12].

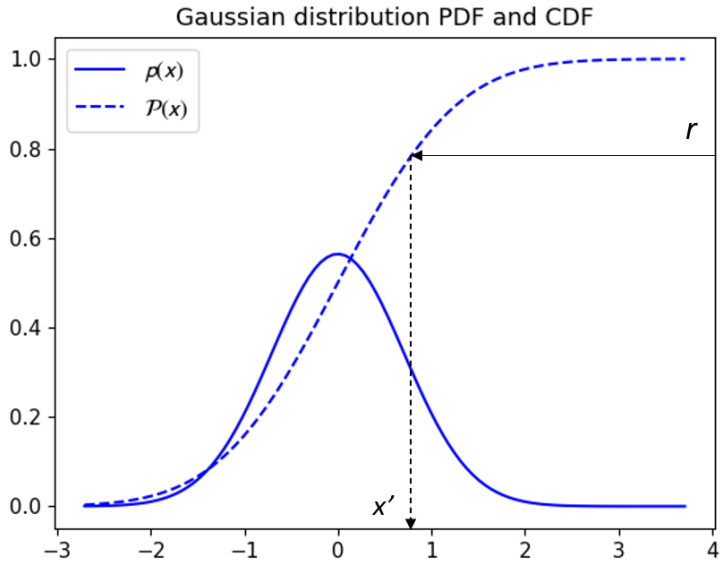

Figure 2.3: The PDF and CDF of a Gaussian distribution. The value of x' can be obtained by taking the inverse of $P(r)$.

2.4.3 The software EGSnrc and egs_brachy

EGSnrc (Electron Gamma Shower National Research Council) is a Monte Carlo code system developed for electron-photon transport and is widely used within medical physics [25]. It has developed throughout the years and there are several additional user codes available, as BEAMnrc [26] and DOSXYZnrc [27]. There are today, moreover, several egs++ (EGSnrc C++ library) applications extending EGSnrc and among these is egs_brachy [28]. This tool uses the advantages from egs++ to model geometries and particle sources specific for brachytherapy. The software is benchmarked against TG43-data for three specific sources and also compared with results from BrachyDose; another software tool to model radiation from brachytherapy sources. The following sections will describe different parts of egs_brachy more in detail.

Cross-sections and particle transport

Within the software, tabulated cross sections are available for different particle interactions and angular sampling. Both photon and electron transport are simulated using these pre-calculated values. To simulate electron transport in detail would result in large simulation times due to the high amount of interactions occurring. Electrons in egs_brachy are therefore transported by use of the Condensed History (CH) technique, introduced by M. Berger in the early 60s [23]. The CH technique is divided into Class I and Class II models where the main difference is the number of events that are grouped together. In Class I, all events are grouped together, while in Class II only a subset of them are grouped. For each condensed history step where grouping is performed, the energy and direction for the primary electron

are sampled from appropriate multiple scattering distributions to take into account the effects of all individual events occurring. The events are therefore not explicitly modelled. In the Class II model, only events above a specific threshold (called catastrophic events) are dealt with explicitly. If photons from bremsstrahlung processes have energy larger than a threshold E_γ or atomic electrons from inelastic scattering having kinetic energy larger than T_c, the transport of the secondary particles will be performed. For the other cases, grouping will be applied. In egs_brachy is the Class II model implemented, but when crossing boundaries between different medium, the default is that no condensed history is performed.

Input file and dose calculation

The input files are text based and make it easy to include wanted geometries and score certain properties like the dose in each voxel, the phase space and the particle tracks. A simulation can be run in normal mode or in superposition mode. If the user wants to simulate a treatment setup with a source stepping between dwell positions, the superposition mode should be selected. When running in superposition mode, a wrapper can be used so that only one dwell position is modelled simultaneously. This is good to prevent overlapping geometries when dwell positions are close to each other. The dwell positions are given as translations and rotations of the source and the corresponding dwell time is expressed by assigning a weight w to each position. Figure 2.4 shows an example of lines in the input file where the run mode is selected and which initial seeds the RNG should use.

```
#-------------------------------
:start run mode:
    run mode = superposition
:stop run mode:


:start rng definition:
    initial seeds = 1000, 200
:stop rng definition:

#-------------------------------
```

Figure 2.4: Example of lines from an input file in egs_brachy. The run mode is selected to superposition to model a source stepping between several dwell positions.

What quantities to score is selected in the scoring section. If phase space scoring is active, the phase space of the current particle will be scored as soon as the particle has left the source surface. The option to kill the particle immediately afterwards can be used to abstain from further particle transport, decreasing the total simulation time. Absorbed dose per history per source or source position in voxel j is calculated as

$$\bar{D^j} = \sum_{k=1}^{N} \frac{D_k^j}{N/n_s} \quad \text{[Gy]}, \tag{2.16}$$

where D_k^j is the dose deposited in voxel j from all particles originating from history k, N is the number of statistically independent histories and n_s the number of sources/source positions. The fractional uncertainty on the dose in voxel j is output per history as

$$s_{D^j} = \sqrt{\frac{1}{N-1}\left[\sum_{k=1}^{N}\frac{(D_k^j)^2}{N} - \left(\sum_{k=1}^{N}\frac{D_k^j}{N}\right)^2\right]} \tag{2.17}$$

Both the dose and statistical uncertainty are output in 3ddose-format, described in the manual for BEAMnrc [26]. To get the absolute dose scored in a voxel, a scaling factor is used. A value of the air kerma strength per history, $S_k^{history}$ for the current source is needed as well as the total radiation time t_{tot}, which is the sum of all dwell times. Air kerma is the energy released in a unit mass of air and $S_k^{history}$ has the unit of Gy·cm^2/history. The absolute dose can be obtained via

$$D^j = \text{TRAK} \cdot \frac{\bar{D}^j}{100 S_k^{history}} \cdot w_{max} \quad \text{[Gy]}, \tag{2.18}$$

where w_{max} is the largest weight among the dwell positions, corresponding to the longest dwell time. TRAK is an acronym for the total reference air kerma in unit cGy cm^2, obtained from the reference air kerma rate (RAKR) in cGy cm^2/h, specific for the used source, times the total radiation time t_{tot}.

The phantom geometry

In egs_brachy there are several predefined geometries to be used for scoring properties such as absorbed dose. The voxel volume can be changed, as well as the boundaries or type of geometry. This alternative is to prefer when scoring dose in a geometry where all voxels having the same material. There is also the alternative to use a file format called *egsphant*. This file format is preferably used when the user wants to score dose in tissue and more patient specific geometries. Each voxel is then assigned one material and one density which is varying over the geometry. However, the volume to score dose in is called phantom in both cases. Figure 2.5 shows a slice of a head-and-neck phantom from an egsphant-file. Each number or letter represent a voxel with an assigned material.

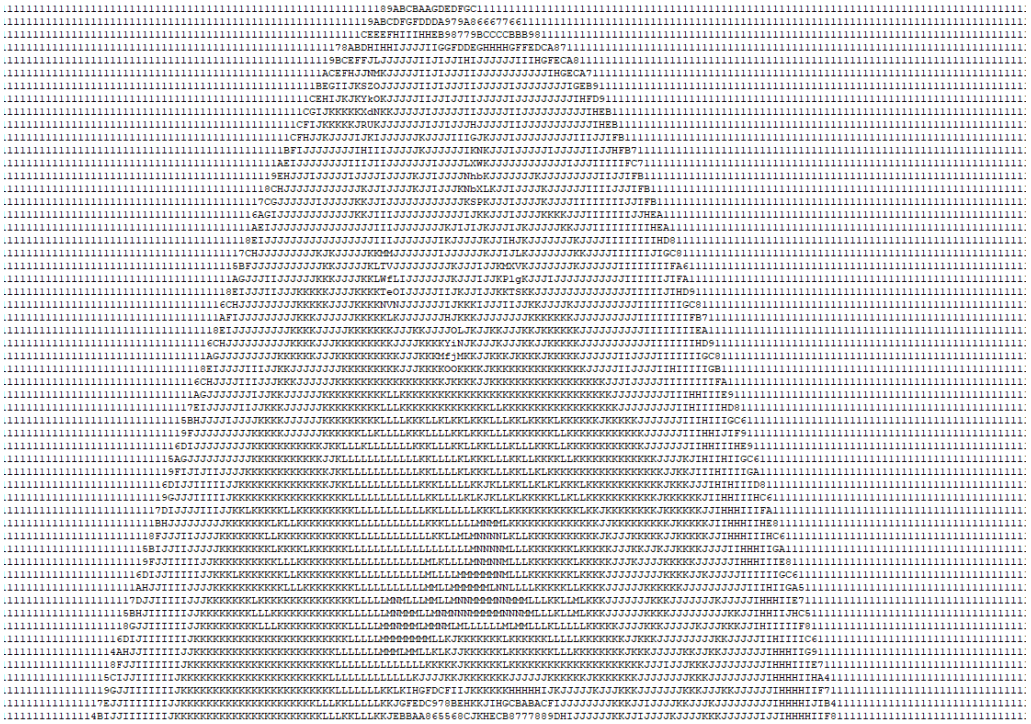

Figure 2.5: A visualization of a head-and-neck-phantom in the format of an egsphant-file. Each number or letter represent a certain material.

3 | Methodology

To start with, a short description of the software setup and the brachytherapy source used will be given. The project's method can thereafter be divided into two parts. The first part will describe the production and analysis of a phase space file. The second part describes the comparison of dose distributions obtained with egs_brachy, TG43 and the brachy Monte Carlo dose engine prototype, which uses the reduced phase space from part one as input.

3.1 Software setup

For all parts of this thesis the following settings can be assumed. The radiation transport code name is egs_brachy, version 2017.09.15 beta with last commit tagged 'bd58535'. The software is compiled using gcc version 9.3.0. The cross section library used for photon transport is XCOM [29]. Photon production from atomic relaxations (K, L, M, N shells) are modelled. Bremsstrahlung cross section is from the NRC data base. In all calculations, the lower and upper thresholds for photon creation are set to 0.001 MeV and 2.012 MeV. Same thresholds for electron creations are set to 0.512 MeV and 1.5 MeV. The random number generator used is RANMAR and the initial seeds are changed from their default numbers when running different simulations.

3.2 The source microSelectron-v2

The specific brachytherapy source is the microSelectron-v2 from Nucletron [30] (acquired by Elekta, Stockholm, Sweden), also called mHDR-v2. It is a cylindrical HDR source with the isotope ^{192}Ir. The tabulated spectrum file Ir192_NNDC_2.6_line.spectrum (included in the the egs_brachy library) is used in the simulations. The source geometry in egs_brachy is modelled to be consistent with dimensions in the study from Daskalov *et al* [30]. The source encapsulation consists of a 0.90 mm diameter AISI 316L stainless steel cylinder with a rounded edge. The radioactive core length is 3.6 mm with a diameter of 0.65 mm. The outer length is 6.5 mm. Figure 3.1 shows how the model looks like in egs_brachy, visualized with the tool egs_view. The z-axis is along the longitudinal direction of the source in the direction of the spherical tip and the x- and y-axes span the transverse plane. Figure 3.2 shows the source design with measures from [6].

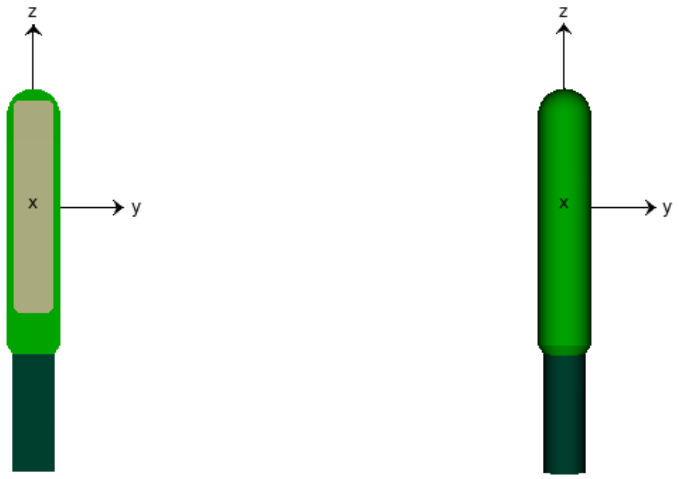

(a) **(b)**

Figure 3.1: The brachytherapy source mHDR-v2 visualized in egs_brachy. (a) shows an intersection of the source, showing the radioactive core. (b) shows a 3D interpretation of the source.

3.3 Design of input data for a brachy Monte Carlo dose engine

3.3.1 Scoring of phase space with egs_brachy

The scoring of the phase space is carried out on the surface of the source geometry. To reduce the number of surfaces and edges of the geometry, the source was placed in a cylinder of air with dimensions 1μm larger in each direction than the source itself. That is, a total length of 6.502 mm and radius of 0.451 mm. Figure 3.3 shows the source placed in the air cylinder. Since the medium in the channels that the source moves within is air, an air cylinder will not make any difference to the radiation properties more than that the phase space is scored a 1μm further away from the actual source. Where the geometry ends, the MC transport with the dose engine will begin. To place the source in an air cylinder facilitated the analysis and made it easier to describe the geometry mathematically.

The cylinder with the source was placed at one single position in origo and an enclosing water box with dimensions 2 cm x 2 cm x 2 cm and voxel size 1 mm^3 was centered around it. The z-axis of the coordinate system was directed along the long axis of the source. The phase space is scored immediately when the particle has exited the cylinder surface and it is therefore sufficient to have a small enclosing phantom around the source. The setting to "kill" the particles was chosen to exclude further particle transport in the phantom and thus reduce the simulation time. A

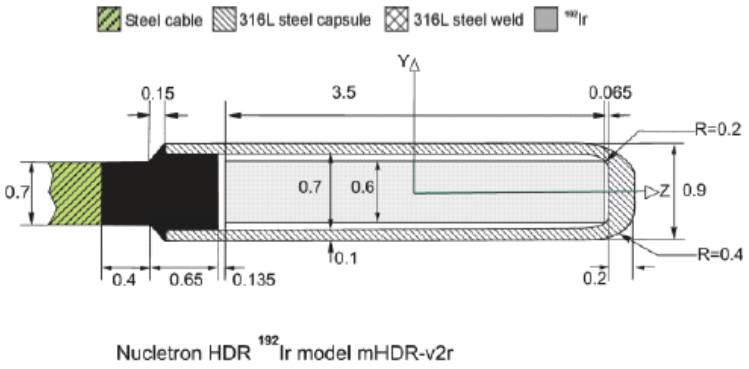

Figure 3.2: Design of the mHDR-v2 from [6]. Dimensions are in millimeter.

simulation with 10^9 initial particles was executed in normal run mode. The resulting phase space file had a size of 22 GB, including information of around $8.1 \text{x} 10^8$ particles that had passed through the surface. A phase space file from egs_brachy is given in IAEA-format [31], which is a standardized format to present particle properties when emerging from a source of radiation. Each particle is only scored once when passing the scoring surface. The phase space file contains eight variables to describe each particle, given in the following order: the sign of directional cosine in z (also representing the particle type), the energy in MeV, three Cartesian position coordinates in cm, two directional cosines (x, y) and a statistical weight.

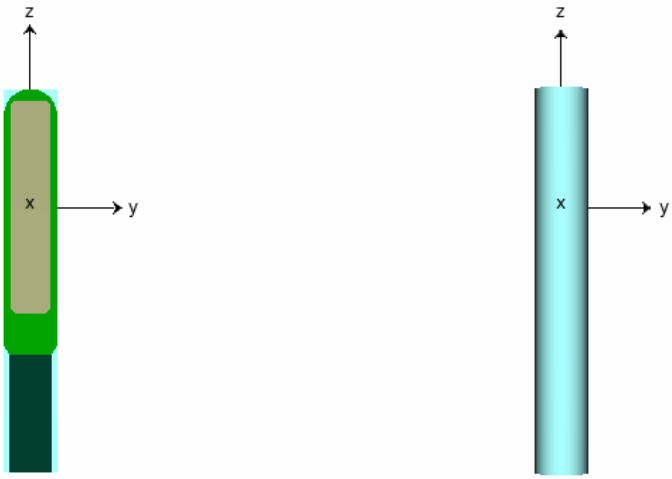

(a) **(b)**

Figure 3.3: An air cylinder around the brachytherapy source mHDR-v2. (a) shows an intersection of the cylinder with the source inside and (b) shows the full cylinder. The cylinder dimensions are 1 μm larger in each dimension than the source itself.

3.3.2 Introduction of new coordinates

To reduce the number of dimensions in the phase space, new coordinates were introduced and all unnecessary variables omitted. The following reductions were done.

Particle type The observed source does only emit photons. The particle type was therefore not stored.

Energy The energy spectrum was saved without any changes.

Position The z position was saved without any changes. Because of the rotational symmetry around the z-axis a uniform distribution can be used for sampling of the x- and y- positions. These variables were therefore excluded in the new phase space file.

Direction A new particle directional vector $\hat{\mathbf{v}}$ was defined, decomposed in two components. The first, $\hat{\mathbf{v}}_{zn}$, is located in the plane spanned by the positive z-axis and the normal vector of the cylinder long side. The other, $\hat{\mathbf{v}}_{xy}$, is located in the transverse plane, spanned by the x- and y-axes. To describe the particle directional vector $\hat{\mathbf{v}}$ two new angle-coordinates were defined. The angle $\theta \in [0,\, \pi]$ represents the angle between the positive z-axis and the component $\hat{\mathbf{v}}_{zn}$, calculated as

$$\cos(\theta) = \frac{\hat{\mathbf{d}} \cdot \hat{\mathbf{e}}_z}{||\hat{\mathbf{d}}||}, \tag{3.1}$$

where $\hat{\mathbf{d}}$ is the directional vector given in the phase space and $\hat{\mathbf{e}}_z$ the unit basis vector of the z-axis. Figure 3.4 shows the θ-angle for a particle located at point P on the cylinder surface.

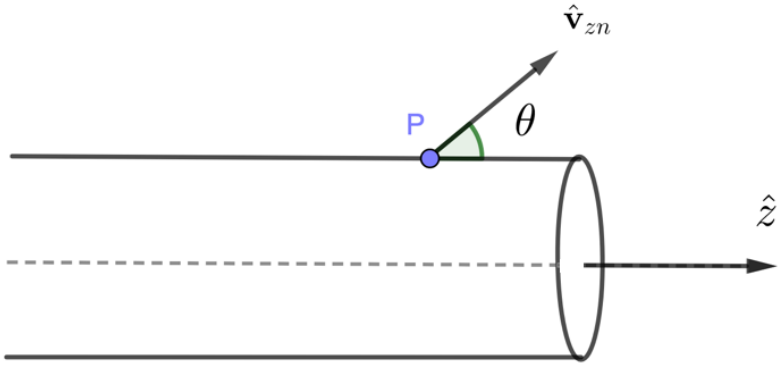

Figure 3.4: The angle θ calculated for a particle at point P with an arbitrary position z.

The angle $\phi \in [-\pi/2,\, \pi/2]$ represents the angle in the transverse plane measured between the directional vector and the normal vector of the long surface, given by

$$\phi = (\phi_{\hat{\mathbf{n}}} - \phi_{\hat{\mathbf{v}}_{xy}}). \tag{3.2}$$

The normal vector is calculated from the position of the particle and the two indexed angles are determined with respect to the positive x-axis as shown in Figure 3.5. The figure is the transversal intersection of the cylinder at the particle position of the cylinder with the angle ϕ calculated at point P for an arbitrary z-value. At every point P, there is a coordinate system of x, y and z to describe the direction of that particle.

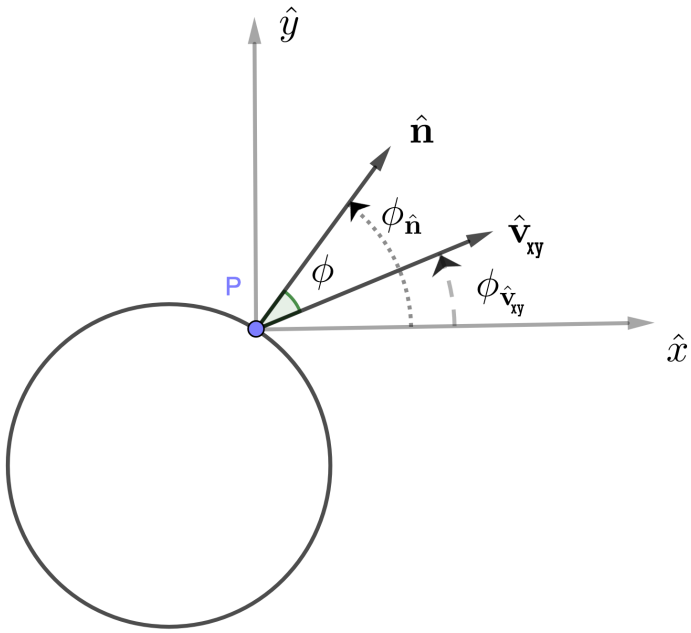

Figure 3.5: The angle ϕ calculated for a particle at point P with an arbitrary position z. The normal vector $\hat{\mathbf{n}}$ and direction vector $\hat{\mathbf{v}}_{xy}$ makes the angle $\phi_{\hat{\mathbf{n}}}$ and $\phi_{\hat{\mathbf{v}}_{xy}}$ with the x-axis respectively.

The angle ϕ is undefined for the flat edges on each short end. The component $\hat{\mathbf{v}}_{xy}$ will instead be sampled uniformly inside the MC for these particles.

In the end, the number of variables were reduced to four, i.e, the energy, position along the z-axis, θ and ϕ angles. These properties assembled over all simulated particles were stored in a 4D-histogram. One bin in the 4D-histogram is representing particles with values in a given range for each property. Not all particles in the same bin have exactly the same properties due to the size of the bins. However, by choosing sizes small enough, particles with similar properties may be grouped together. The dimensions and bin sizes of the 4D-histogram can be seen in Table 3.1. The minimum and maximum represent the first and last bin edge of each dimension. These are set to the minimum and maximum of the resulting particle energies for the energy dimension. Two extra bins have been added to the z position. They correspond to the particles with location at one of the two flat surfaces. The

distinction of which of the three surfaces a particle is located on was done by first checking the radial position followed by the z position.

Table 3.1: Dimensions of the 4D-histogram. Min and max represents the first and last bin edges for each dimension. The z position has 2 extra bins corresponding to the two flat surfaces on each side of the cylinder.

Variable	Min	Max	Bin size	Number of bins
z position	-4.502 mm	2.002 mm	≈ 0.1 mm	67
θ	0	π	0.052 rad	61
ϕ	$-\pi/2$	$\pi/2$	0.052 rad	61
Energy	0.005 MeV	1.373 MeV	≈ 10 keV	137

All parsing and processing of data was done with Python 3, using the libraries `numpy` and `struct`. The 4D-histogram was analyzed by plotting the variables both globally by summing over all dimensions except for the one analyzed, and also locally where the summation was done over certain values. The goal was to see how the distributions of the parameters changed as a function of the energy and z position along the source. This 4D-histogram could now be used as a reduced phase space file for the brachy Monte Carlo dose engine to sample from.

3.4 Comparison of dose distributions

This section will describe the procedure to score the absorbed dose from two different treatment plans in water and in material with the simulation tool egs_brachy. Further, the same treatment plans will be used to calculate absorbed dose with the two dose engines in RayStation; TG43 and the brachy Monte Carlo prototype. Eventually, the method for comparison of the dose distributions will be described.

3.4.1 Determination of dwell positions and dwell times in egs_brachy

The dwell positions of each plan were directly imported to the egs_brachy-format from the DICOM RTPlan via a python script and the library `pydicom`. The coordinates were given from the attribute "Control Point 3D Position" as

$$x_{EGS} = \frac{x_{DICOM}}{10}, \tag{3.3}$$

$$y_{EGS} = \frac{y_{DICOM}}{10}, \tag{3.4}$$

$$z_{EGS} = \frac{z_{DICOM}}{10}, \tag{3.5}$$

due to the dimension change from millimeter in DICOM to centimeter in egs_brachy. The source rotation was calculated from the directional cosines stated in the DICOM-file under the attribute "Control Point Orientation". The rotational angles α and β

around $\hat{x}$ and $\hat{y}$ respectively, are determined via the equations

$$\alpha = \arccos\left(\frac{\cos c}{\cos \beta}\right) \tag{3.6}$$

$$\beta = \arcsin\left(-\cos a\right), \tag{3.7}$$

where the values cos a and cos c are the directional cosines for x and z, given from the treatment plan. Due to arccos can give + or - the equation $\cos b = \cos\alpha \cdot \cos\beta$ is used to determine the correct sign of the angle α. Here cos b is the directional cosine for y. A manual check by viewing the rotations with the tool egs_view in EGSnrc was performed to ensure correctness. The equations are derivable from the rotational matrix of the convention in egs++ [32].

3.4.2 Scoring of dose distributions with egs_brachy

The same input file in egs_brachy was used as base for all cases investigated. What was changed between them were the phantom geometry and plan specific settings, such as dwell positions, dwell times and dose scaling factor. For the cases with a non-homogeneous phantom, an egsphant-file was used where the materials for each voxel were directly exported from RayStation. In the TPS, a mass density is first assigned to each voxel via conversion of Hounsfield Unit-values from the CT-images according to a CT calibration curve. The mass density is then mapped to a material by finding the material with the closest matching mass density [33]. The material mapping step includes 55 different materials whose values are interpolated from 10 well-established tissue compositions taken from ICRU report 24 and ICRP 23. The dimension of the dose grid was set in the TPS and exported together with the densities and material assignment to an egsphant-file via a python script. The compositions and densities of the 55 materials were also added to a data file to be used during simulations. However, the mean ionization energy (I-value) for each material was not possible to easily include in the simulations. They were instead calculated within the software with help of the material composition, leading to slightly different values than in the TPS.

Head-and-neck: water The phantom size was 16 x 20 x 16 cm^3 with a voxel volume of 1 mm^3 and all voxels made of water with a density of 0.998 g/cm^3. The water phantom was placed in a larger water cube of size 30 x 30 x 30 cm^3 to get full scatter conditions. 117 different dwell positions were included in the plan. Total number of histories simulated was $4 \cdot 10^{10}$.

Head-and-neck: material The phantom size was 20 x 16 x 18 cm^3 with a voxel volume of 1 mm^3. Each voxel was assigned the material used in dose calculation with the TPS. The number of different materials used was 54. The phantom was placed in a larger air cube of size 30 x 30 x 30 cm^3 to model a clinical setup with air outside the patient. 117 different dwell positions were included in the plan. Seven different simulations were run and combined by taking the average of their dose distributions. Total number of histories was $7 \cdot 10^{10}$.

Breast: water The phantom size was 14 x 12 x 12cm^3 with a voxel volume of 1 mm^3 and all voxels made of water with a density of 0.998 g/cm^3. The water phantom was placed in a larger water cube of size 30 x 30 x 30 cm^3 to get full scatter conditions. 491 different dwell positions were included in the plan. Two different simulations with $2 \cdot 10^{10}$ number of histories were run and combined by taking the average of their dose distributions. Total number of histories was $4 \cdot 10^{10}$.

Breast: material The phantom size was 14 x 12 x 12 cm^3 with a voxel volume of 1 mm^3. Each voxel was assigned the material used in dose calculation with the TPS. The number of different materials used was 48. The phantom was placed in a larger air cube of size 30 x 30 x 30 cm^3 to model a clinical setup with air outside the patient. 491 different dwell positions were included in the plan. Three different simulations were run and combined by taking the weighted average of their dose distributions. Total number of histories was $8 \cdot 10^{10}$.

The dose distributions were output in 3ddose-format [26]. An RTDose file connected with the current used RTPlan file was copied via a python script and the dose scored with egs_brachy was attached to the copy. The dose could then be imported in the TPS for comparison with dose distributions computed with the TPS RayStation itself. The prototype of the brachy Monte Carlo dose engine used the reduced phase space file to sample photons from and dose distributions were calculated with 10^{10} number of histories.

3.4.3 Methods for comparison of dose distributions

The results from the simulations with egs_brachy was used to compare calculations done with the two brachytherapy dose engines in the TPS RayStation®. The comparison of dose distributions was first carried out with the gamma evaluation method [34]. This is a method that combines two important measures into one: the dose difference tolerance ΔD and the distance-to-agreement (DTA). The dose difference tolerance is the accepted relative dose difference and can be in percent of a local dose value, e.g. the dose at each evaluated point, or a global reference dose value, e.g. a dose maximum. The DTA is defined as the minimum distance between a data point in one dose distribution and a data point in the other dose distribution that show the same dose level. The criterion can be set to Δr for the DTA. The two dose distributions to be compared will further be referred to as the reference dose $D_r(\mathbf{r})$ and the comparison dose $D_c(\mathbf{r})$, at point $\mathbf{r}$ in the dose distribution. A quality index (called gamma value) at each point is used for evaluation, defined as

$$\gamma(\mathbf{r}_r) = \min\{\Gamma(\mathbf{r}_r, \mathbf{r}_c)\} \; \forall\{\mathbf{r}_c\} \tag{3.8}$$

where

$$\Gamma(\mathbf{r}_r, \mathbf{r}_c) = \sqrt{\left(\frac{r}{\Delta r}\right)^2 + \left(\frac{\delta}{\Delta D}\right)^2}. \tag{3.9}$$

Here $r = |\mathbf{r}_c - \mathbf{r}_r|$ is the distance between the points in each dose distribution and

$\delta = D_c(\mathbf{r}_c) - D_r(\mathbf{r}_r)$, the dose difference at the same points. Points for which $\gamma \leq 1$, given the values of ΔD and Δr, are said to pass the gamma criteria.

Two different local gamma criteria were used. One with $\Delta D = 1\%$ of the local reference dose and $\Delta r = 1$ mm, written as (1%/1 mm), and another with criterion (3%/2 mm). The maximum fail rate to compare with for the two cases was set to 2% and 10% respectively. That means that some of the points are allowed to not pass the criterion but the total dose distribution could still pass the gamma test. The dose calculated with egs_brachy was always used as reference dose.

Another, more illustrative comparison, was also carried out by plotting line doses of the different dose distributions along one direction. Additionally, 2D-plots showing the dose difference between two dose distributions were visualized in the TPS.

The dose scored with the TG43 dose engine was compared with the dose distribution calculated with egs_brachy for both water cases. The dose distributions calculated with the brachy Monte Carlo dose engine were compared with the simulated head-and-neck case and the breast case in material.

4 | Results and Discussion

This chapter will present the results from the phase space analysis and the comparison of dose distributions. A discussion of the results is also included. Different parts of the source will be referred to as head, tail and long side. The tail is the bottom part of source, connected to the cable. The head is the top part with the spherical tip. The long side will referred to the whole long side of the cylinder. This is illustrated in Figure 4.1.

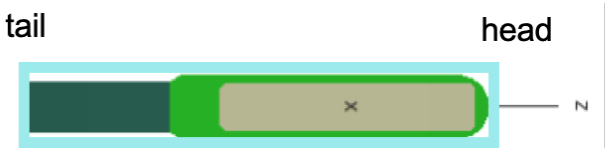

Figure 4.1: Definition of tail and head part of the source.

4.1 Phase space analysis

The introduced parameters, energy, z position, ϕ and θ were carefully examined. To study dependencies and distributions of certain parameters, a summation over the other dimensions was performed.

Figure 4.2 shows the distribution of photon locations along z. An illustration of mHDR-v2 is inserted to give a better overview of the dimensions. The majority of photons are positioned in the middle part -0.18 cm $\leq z \leq$ 0.17 cm where the isotope is located. The number of photons has decreased towards the tail, due to the shielding material and the distance from the radioactive part. The individual bin with highest number of photons is the one representing the head part. However, this bin includes a larger area than the bins on the long side since the full flat edge is covered.

Figure 4.3 shows the energy spectrum divided in the three parts: head (red), tail (yellow) and long side (blue). The normalization is done separately for each part. The flat edge closest to the cable connection has a slightly higher ratio of photons with energies higher than 0.45 MeV compared with the other two sides. Overall, the energy is assumed to not have a significant z dependency and the same energy spectrum could be used for all z positions.
Figure 4.4 shows the z dependence for the angle θ. This is visualized in Figure 4.4a over the three surfaces. Figure 4.4b shows the z dependence of the cylinder long side

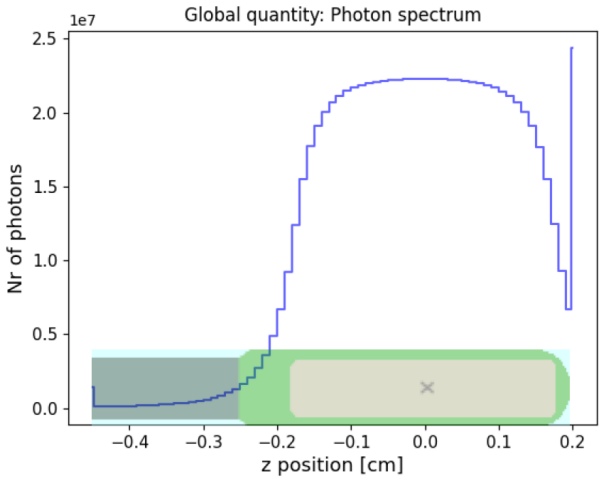

Figure 4.2: Distribution of photons along z-axis. The majority of photons are close to the radioactive part of the source.

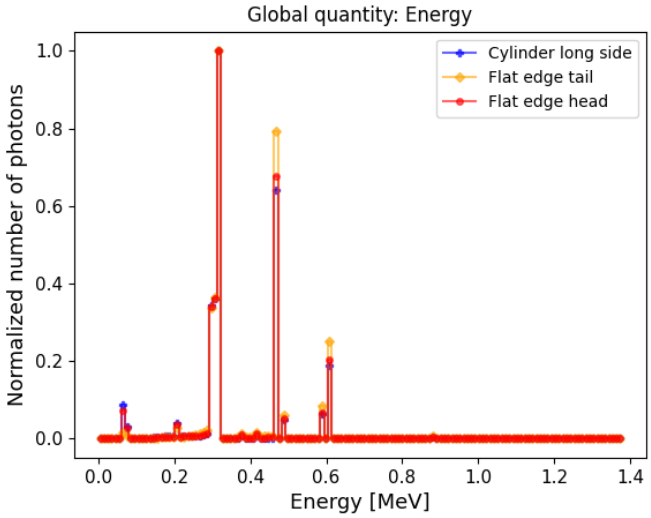

Figure 4.3: The energy spectrum showing the distribution of photon energies over the source.

but summed over different z-ranges. Figure 4.4c is included to get a better overview of the z positions along the source. The two dashed lines in (a) represent the flat edges. θ follows a Gaussian distribution centered around $\pi/2$ when summing over the cylinder long side. This was expected due to the isotropic emission from the isotope and the thin shielding around the radiating part. The most probable angle with relation to the z-axis should then be $\pi/2$; the direction pointing outwards. Also the tail and head flat edge show distributions where the direction is pointing out from the surface. As can be noted in Figure 4.4a and confirmed in Figure 4.4b, the distribution goes from π rad towards 0 rad when following the source from tail part (negative z) to the head (positive z). The regions corresponding to the red and green lines in Figure 4.4b are covering the full radioactive part of the source. It is only a

small shift between their positions while as soon as the radioactive part ends, shown with the yellow and black lines, the shift starts to increase. The distribution is no longer centered around $\pi/2$. It is necessary to at least have different θ-distributions to model the three distinct surfaces, as shown in Figure 4.4a. For a more detailed distinction, the long side could also be divided into different distributions as shown in Figure 4.4b; using Gaussian distributions with certain parameters for the middle part z ∈ [-0.19 cm, 0.15 cm).

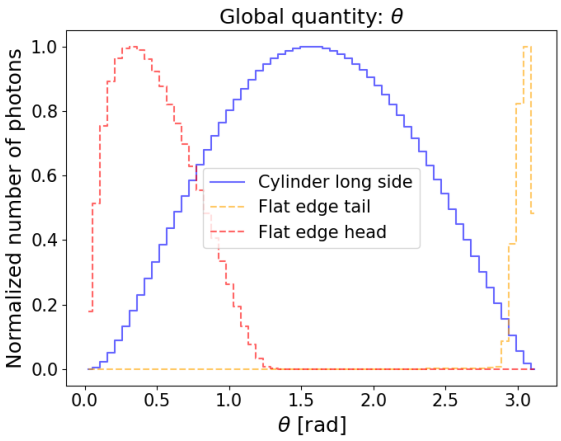

(a) Theta distribution for the three surfaces.

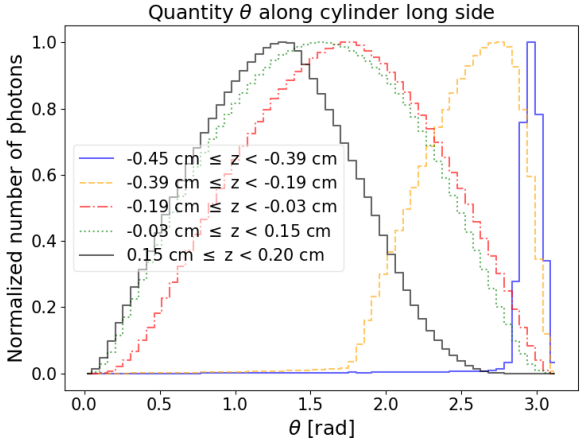

(b) Theta distribution along cylinder long side for different z.

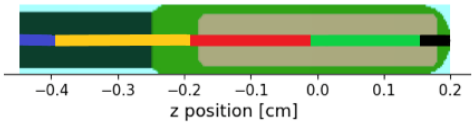

(c) Z positions along the source. Each z range in (b) is marked with its corresponding color.

Figure 4.4: Distributions of the θ angle. They are divided into the two flat surfaces and the cylinder long side along z-axis.

Figure 4.5a shows the z dependence for the ϕ-angle of the cylinder long side. The distribution is similar to a normal distribution centered around 0 rad. In Figure 4.5b, the cylinder long side is divided into different regions with respect to z. Figure 4.5c is included to get a better overview of the z positions along the source. The green dotted line in Figure 4.5b corresponds to the z positions where the radioactive core is located. As can be seen, this distribution is similar to the global one shown in (a). The distribution changes slightly depending on the distance from the radioactive part, but stays symmetric around 0 rad. As mentioned before, the angle ϕ is undefined for the two flat edges and the directional vector component $\hat{\mathbf{v}}_{xy}$ will instead be uniformly sampled within the brachy Monte Carlo dose engine. Initially, it will be assumed that all particles on the flat edge are located at the center. This could be a valid approximation because of the small dimensions and the fact that the photon density is as largest close to the center. This can be seen in Figure 4.6 where around

45% of the photons are enclosed within a circle with radius 0.0015 cm. However, the approximation should be investigated in more detail in future work and might be subject to change.

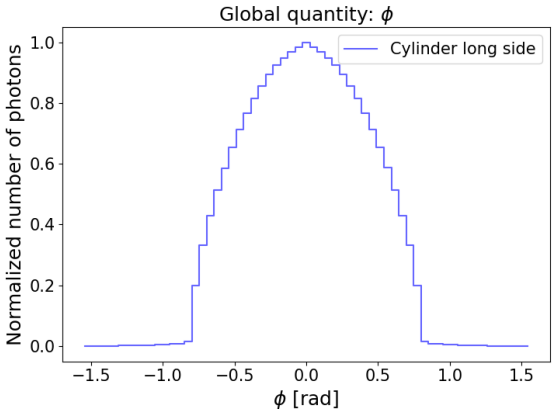

(a) Phi distribution of cylinder long side.

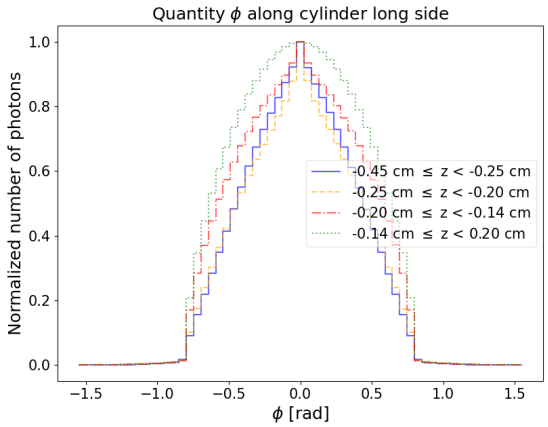

(b) Phi distribution along cylinder long side for different z.

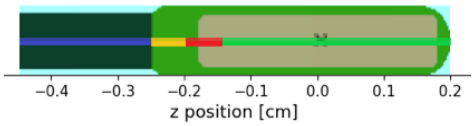

(c) Z positions along the source. Each z range in (b) is marked with its corresponding color.

Figure 4.5: Distributions for ϕ: (a) shows the distribution summed over full cylinder long side, (b) shows the distribution divided into four different z-regions along the cylinder long side, (c) shows each range with its corresponding color.

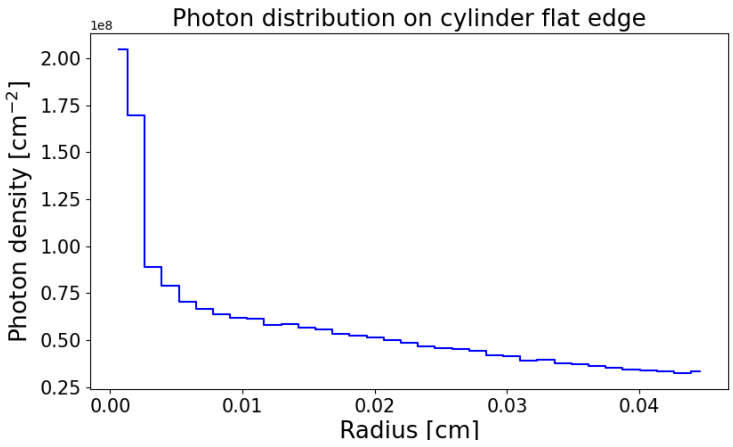

Figure 4.6: The area density of photons at different radii of the flat edges.

Figure 4.7 shows the energy dependence for the photon distribution along the source. There are five energy regions where the start and stop of each region, except for the first, is marked with a dashed line in the sub-figure to the left. As can be seen in

the right sub-figure, the photon spectrum does not have an energy dependency and the same distribution of photons can be assumed for all energies.

Figure 4.8 and Figure 4.9 show the energy dependence for θ on the cylinder long side and the two flat edges, respectively. The same energy regions as shown to the left in Figure 4.7 are used and the energy E_p refer to the photon energy. From the figures it can be seen that θ follows the same distribution for all energy regions except for the low energy region in the case of the cylinder long side (Figure 4.8) and the head part (Figure 4.9a). The shift starts slightly in the range $0.23 \leq E_p < 0.36$ MeV shown in yellow, but is clearer in the lowest energy region, shown in blue. Note that all regions have the same division of 10 keV bins. It could be necessary to have smaller bin sizes for the lowest energy region to capture the full energy dependence.

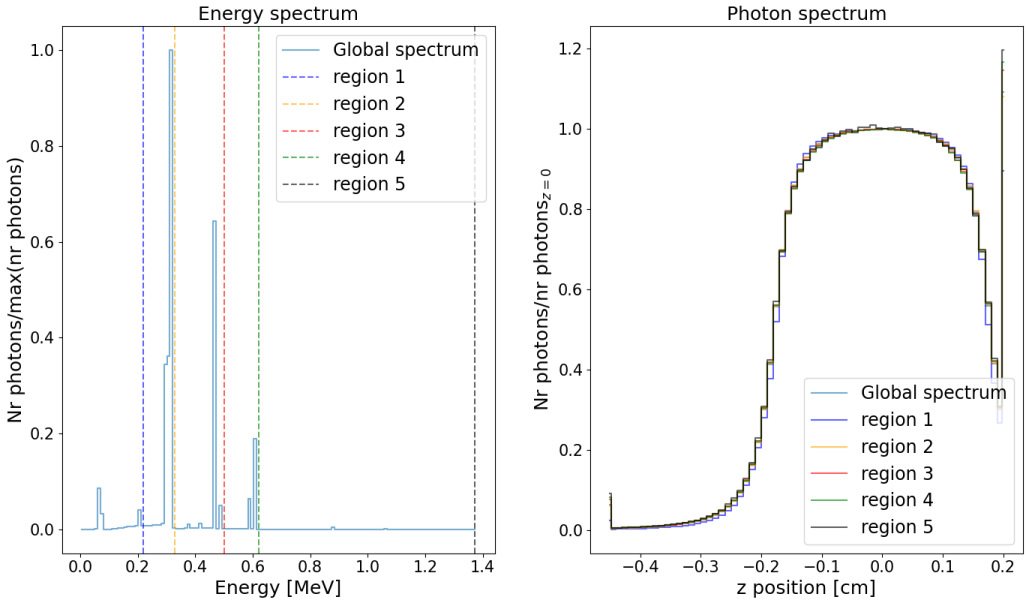

Figure 4.7: The photon spectrum divided into five energy regions. No energy dependence can be seen.

In Figure 4.10, the energy dependence of ϕ for the cylinder long side is presented. As for the θ-angle, it can be seen that the lower energy region has a somewhat different distribution than the others. The difference for the energy range $0.23 \leq E_p < 0.36$ MeV shown in yellow is though less distinct for ϕ than for θ.

When producing a reduced phase space, it is a balance between having enough information to be able to use the phase space in a dose engine and the memory it is needed to store the information. In this case, the file size was reduced from 22 GB to ∼130 MB. From the analysis of the ϕ-distribution, it was found that the distribution always is symmetric around 0 radians. By only storing values of $|\phi|$ and then make a uniform sampling of the sign, the file size could be reduced even more.

Different distributions from the 4D-histogram have been presented in this result section. Possible divisions due to dependencies among the dimensions could be

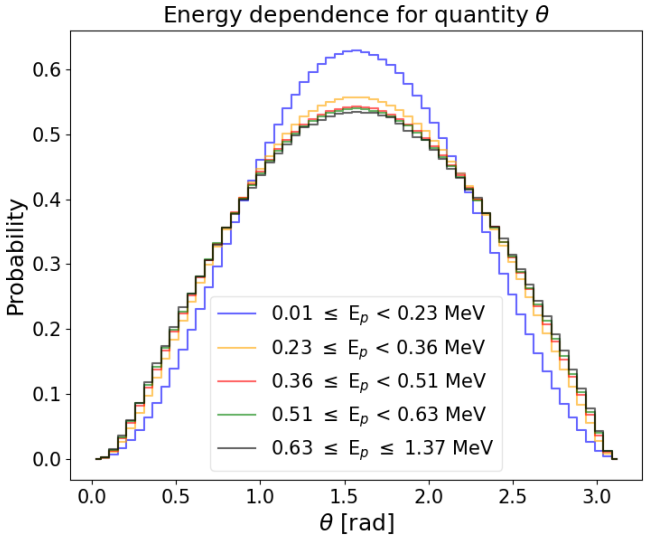

Figure 4.8: The energy dependence of θ along the cylinder long side.

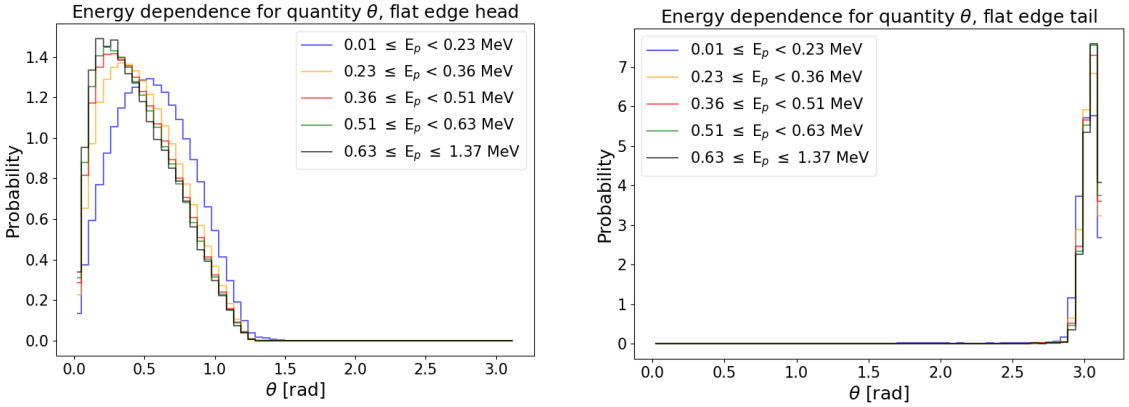

(a) The energy dependence of θ for the head part of the cylinder.

(b) The energy dependence of θ for the tail part of the cylinder.

Figure 4.9: Distributions of the θ-angle with respect to different energy regions.

found. These distributions may later be used as starting point for the MC dose engine via parameterization according to the distributions, and in turn lead to lower amount of memory used to store the information. However, given that the file size already was reduced to the order of 100 MB, it was decided to include and directly sample from the 4D-histogram in the dose engine. In that sense, there is currently no need of parameterization of the distributions for all parameters and the reduced phase space can be seen as the distribution to sample from. The performed analysis is still of importance to understand the characteristics of the radiation from the studied source and for a possible parameterization in the future.

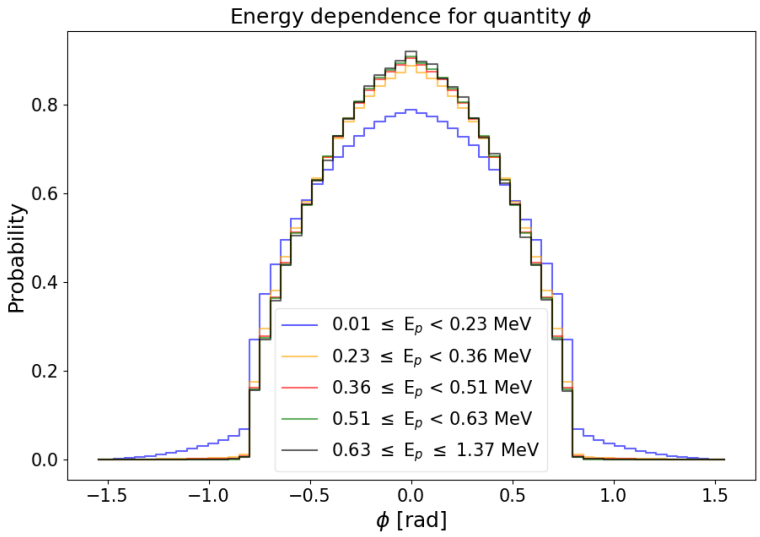

Figure 4.10: The energy dependence of ϕ along the cylinder long side.

4.2 Comparison of dose distributions calculated with RayStation® and egs_brachy

This section will present the results from the performed dose comparisons. The results are divided according to the two patient cases investigated, starting with the head-and-neck case followed by the breast case. The TG43 dose engine is compared with dose distributions computed with egs_brachy in water while the brachy Monte Carlo dose engine (here denoted BMC) is compared with dose distributions computed with egs_brachy in material.

4.2.1 Head-and-neck case

Table 4.1 presents the fail rates from the gamma evaluation for the head-and-neck case. Both TG43 and BMC pass the tests with low fail rates. As a comparison, the allowed fail rate specified in the formal dose engine validation for RayStation [33] is set to 10% for gamma test (1%/1 mm) and 2% for gamma test (3%/2 mm). The favorable gamma results show that both TG43 and BMC can reproduce the simulated dose distributions from egs_brachy well.

Table 4.1: Results from the dose comparisons for a head-and-neck case. The table shows the fail rates of the gamma evaluation.

Test case water	**γ >1.0 (1%/1 mm)**	**γ >1.0 (3%/2 mm)**
egs_brachy - TG43	0.30%	0.01 %
Test case material		
egs_brachy - BMC	1.38 %	0.19 %

Figure 4.11 shows a 2D-plot of the dose difference between TG43 and egs_brachy from two views of the head-and-neck case. The transversal view in Figure 4.11a

and the sagittal view in Figure 4.11b. The dose difference is calculated as D_{TG43} - $D_{\text{egs\_brachy}}$ and it can be seen that the dose distributions follow each other well. Note that it is the absolute difference reported in percent of 100 cGy. It is clear that the largest differences are concentrated close to the dwell positions. This is also illustrated in Figure 4.12 which shows two line doses, one horizontal to the left and one drawn vertical to the right. The location of the lines are shown in Figure 4.12b. In the horizontal dose line, a drop in the dose level for egs_brachy can be seen. This is due to the size of the dose grid that did not reach out to the external. In the vertical dose line in Figure 4.12a, slightly deviating dose levels can be seen in the peak that appears when the line is close to a dwell position. The difference in dose level close to a dwell position is probably due to the handling of the dose values close to or within the source. The TG43-formalism has a singularity in the form of a line segment at the center of the source. In the TG43 dose engine in RayStation, this is handled by an avoidance region, where the dose level within the region is set to the same value as on the surface of it. In egs_brachy, volume correction is instead used. The voxels containing a part of the source geometry will get an adapted volume where the volume of the source part is subtracted. This corrected voxel volume is then used in the dose calculation. Something to keep in mind is also that the doses and gradients are very high close to the source. The absolute dose difference between two dose distributions could therefore be quite large while the relative difference is not significant.

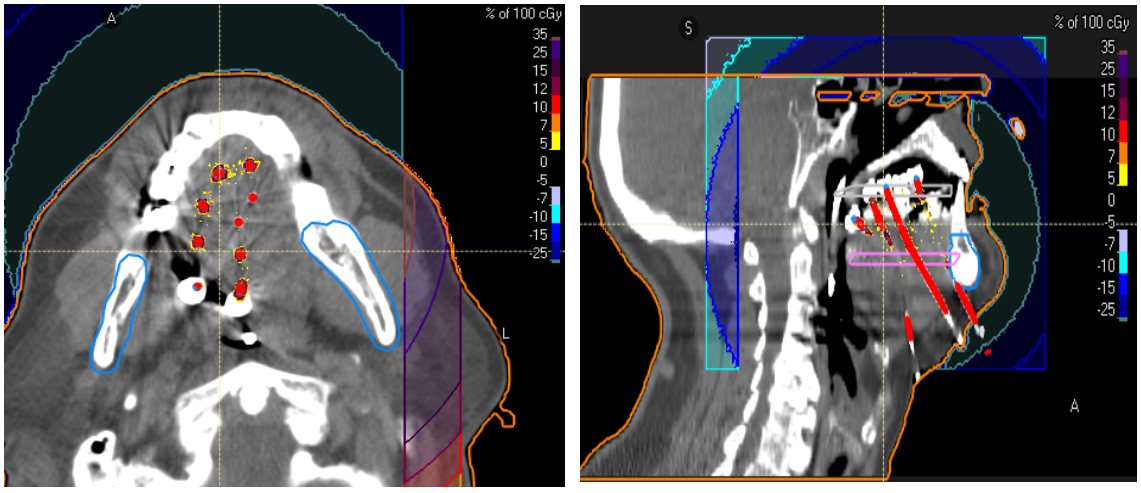

(a) Dose difference transversal view. **(b)** Dose difference sagittal view.

Figure 4.11: 2D-plots of dose difference in water between TG43 and egs_brachy.

In Figure 4.13, two dose lines are plotted for dose scored in material together with the relative dose differences along each line. Note the different scales on the y-axes for the difference plots. Figure 4.14 shows the location of the dose lines in the patient. The lines are drawn in the transversal view, one in horizontal direction and the other line in the vertical direction. The two orange squares in Figure 4.14 mark regions where a representative limitation of the water approximation done by TG43 can be seen. This appears as a sharper bump in the line doses plotted in Figure 4.13. Both the BMC and egs_brachy report a higher dose than the TG43

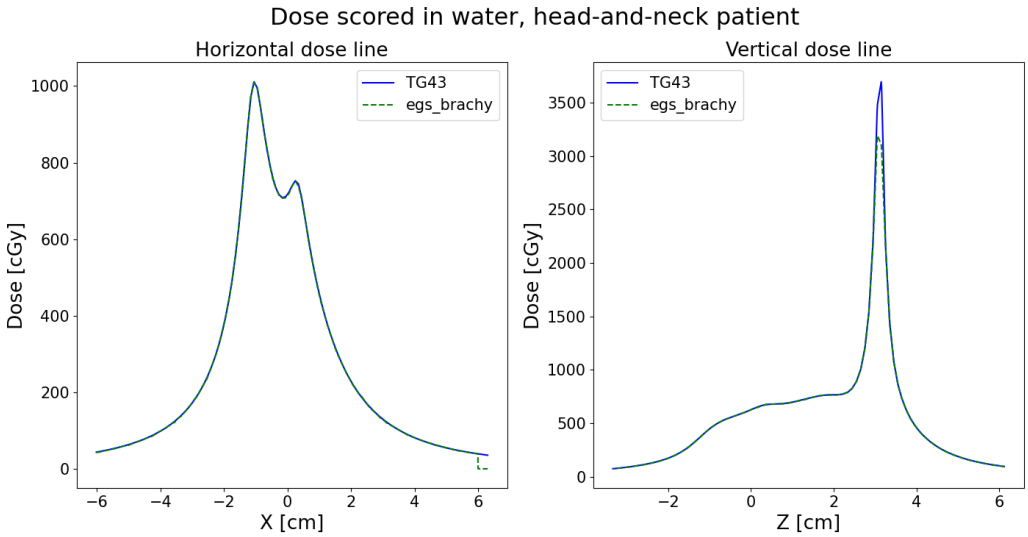

(a) Line doses for TG43 and egs_brachy scored in water.

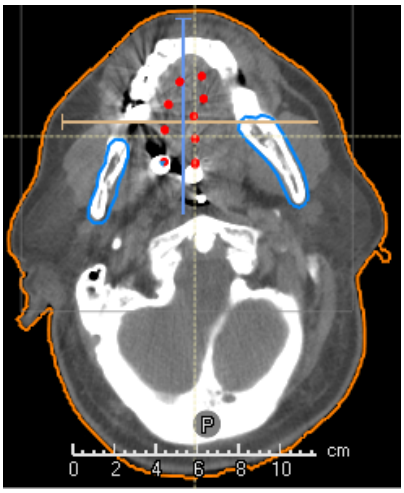

(b) Visualization of the two line doses plotted in Figure 4.12a.

Figure 4.12: Line doses for dose calculated with TG43 and egs_brachy in water.

due to the presence of denser material. The relative dose difference between TG43 and egs_brachy (yellow solid line) at these sites is 15-20% while it is around 2% in the center of the dose lines. The size of the difference is also increasing when approaching the interface skin–air. The dose difference between egs_brachy and BMC (red dashed line) fluctuates close to 0 but tends toward ±4% when approaching a dwell position. Also the BMC has a currently different dose handling at the dwell positions compared with egs_brachy, which can explain the discrepancy.

4.2.2 Breast case

Table 4.2 presents results from the gamma evaluation for the breast case. Also for this case, both TG43 and BMC pass the tests with low fail rates. In Figure 4.15, a 2D-plot of the absolute dose difference in material between BMC and egs_brachy is shown. The difference is calculated as D_{BMC}-$D_{\text{egs\_brachy}}$. It can be seen that the differences for regions not close to the dwell points are less than 5 cGy with large areas having a difference below 2 cGy. The dose levels at these sites are in order of 100 cGy, meaning there is a small relative dose difference. In Figure 4.17, two dose lines together with the relative dose difference between egs_brachy and the two dose engines TG43 and BMC are plotted. The locations of the dose lines are visualized in Figure 4.16. The relative difference between BMC and egs_brachy is here close to 0 and does not exceed 4% for dose line 2. In dose line 1, the difference in dose level close to a dwell position is once again present, hence being larger than 4% at this point. TG43 estimates a higher dose than the two MC-codes in the zoomed-in part in dose line 1. This difference is due to the fact that the dose is reported in two different media and the dose level could be corrected with a factor representative for the material. That the difference gets larger closer to the breast bone and lung, as well as the skin–air interface is again a result of the TG43 limitations.

Table 4.2: Results from the gamma evaluation for a breast case.

Test case water	γ **>1.0 (1%/1 mm)**	γ **>1.0 (3%/2 mm)**
egs_brachy - TG43	1.28%	0.04 %
Test case material		
egs_brachy - BMC	4.29%	0.43%

The results clearly show the difference between a MC-based dose calculation and the TG43 formalism. The gamma values for the two cases presented indicate that both dose engines have a low fail rate. There are some differences between the BMC prototype and egs_brachy that could be due to different transport parameters or scattering conditions. Also the material handling is somewhat different between the two codes, especially at sites where the density is equal to zero. Here, the BMC does not score dose while egs_brachy still does due to an error occurring when having voxel densities lower than 0.001 g/cm^3. This error probably occurs due to a parsing issue of the egsphant file. The I-values are also slightly different as mentioned in the method section. Something to keep in mind when comparing the doses is also the statistical uncertainty for an MC, depending on the number of histories simulated, and its fluctuating nature.

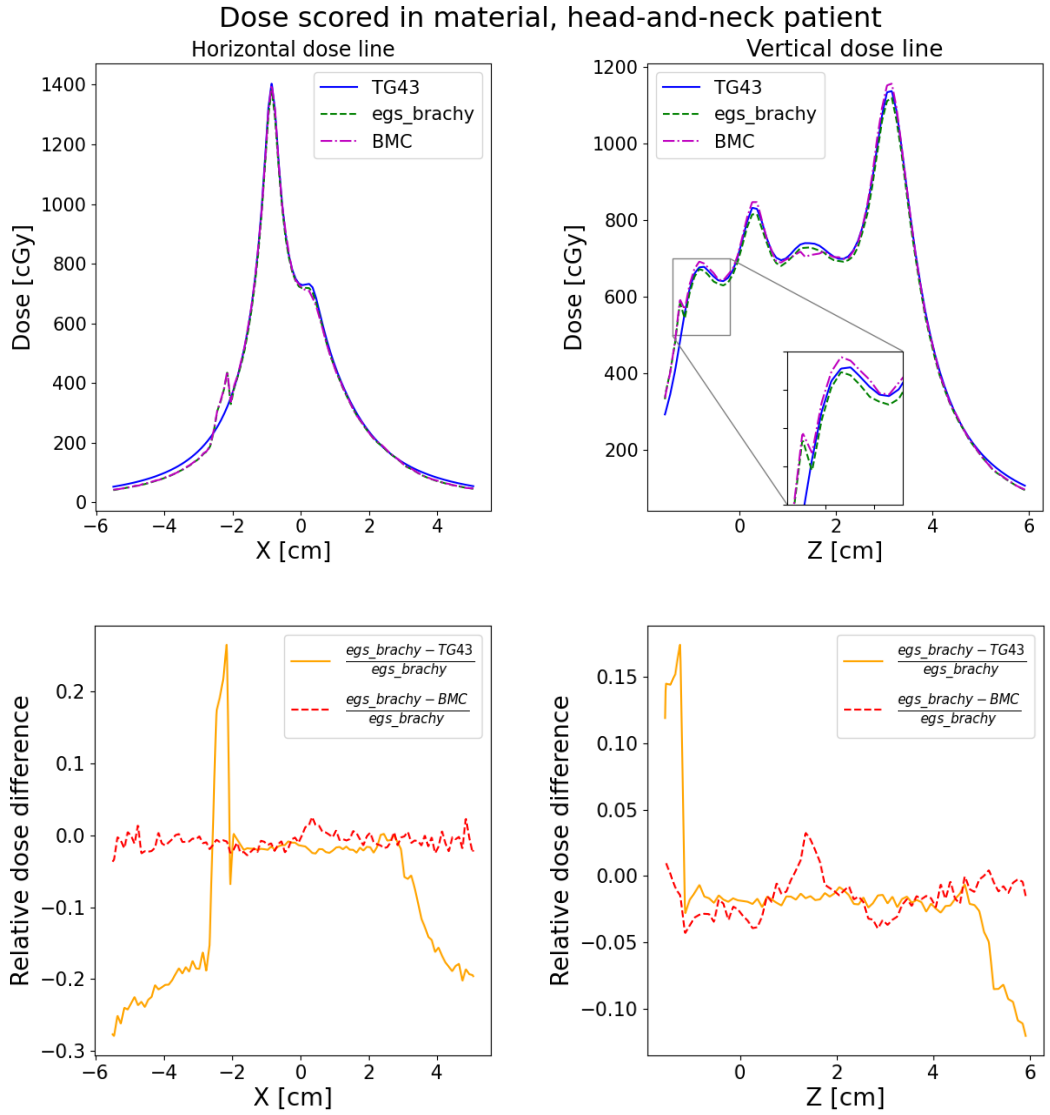

Figure 4.13: Line doses showing the dose scored in material by egs_brachy and BMC. Dose scored in water with TG43, for the same head-and-neck case, is also included. The bottom part shows the relative dose difference between egs_brachy and the two dose engines. Note the different scales on the y-axes for the dose differences.

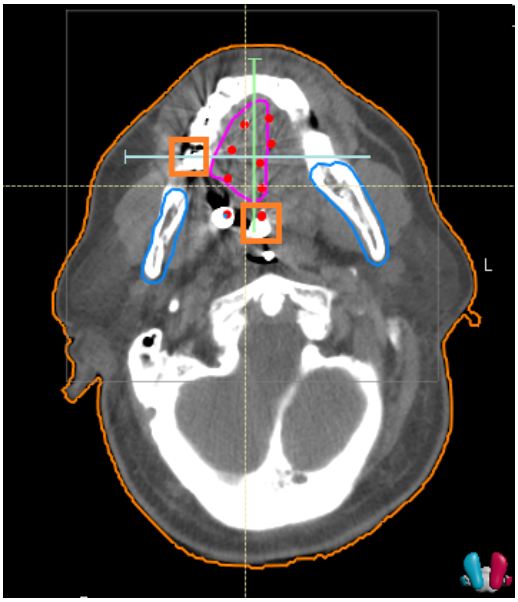

Figure 4.14: Visualization of the two dose lines plotted in Figure 4.13. The orange squares show where the lines pass through dense material.

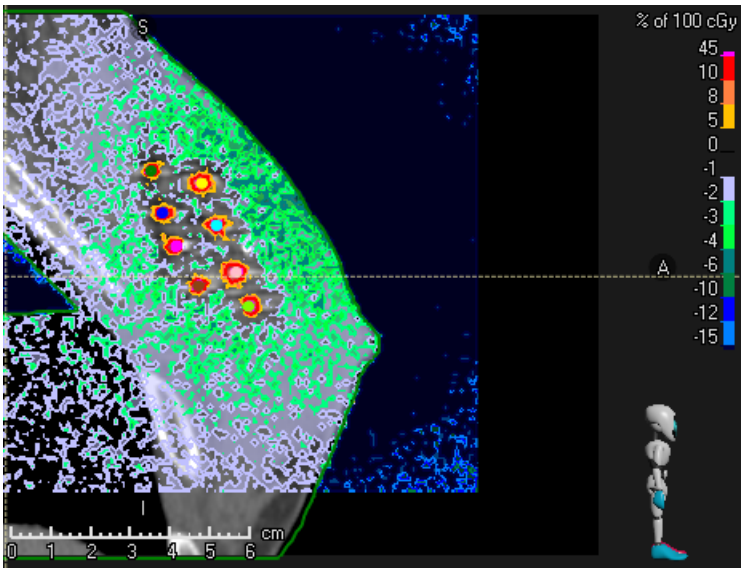

Figure 4.15: Dose difference in material between BMC and egs_brachy.

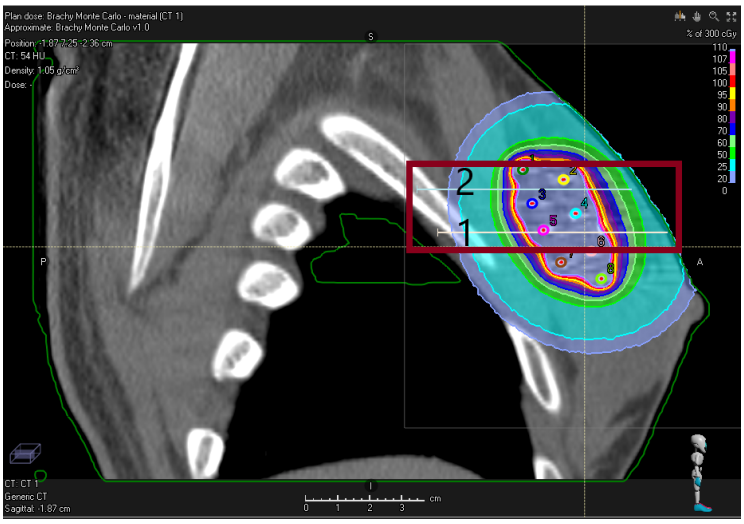

Figure 4.16: Visualization of position for two line doses, marked with a rectangle. The doses are plotted in Figure 4.17.

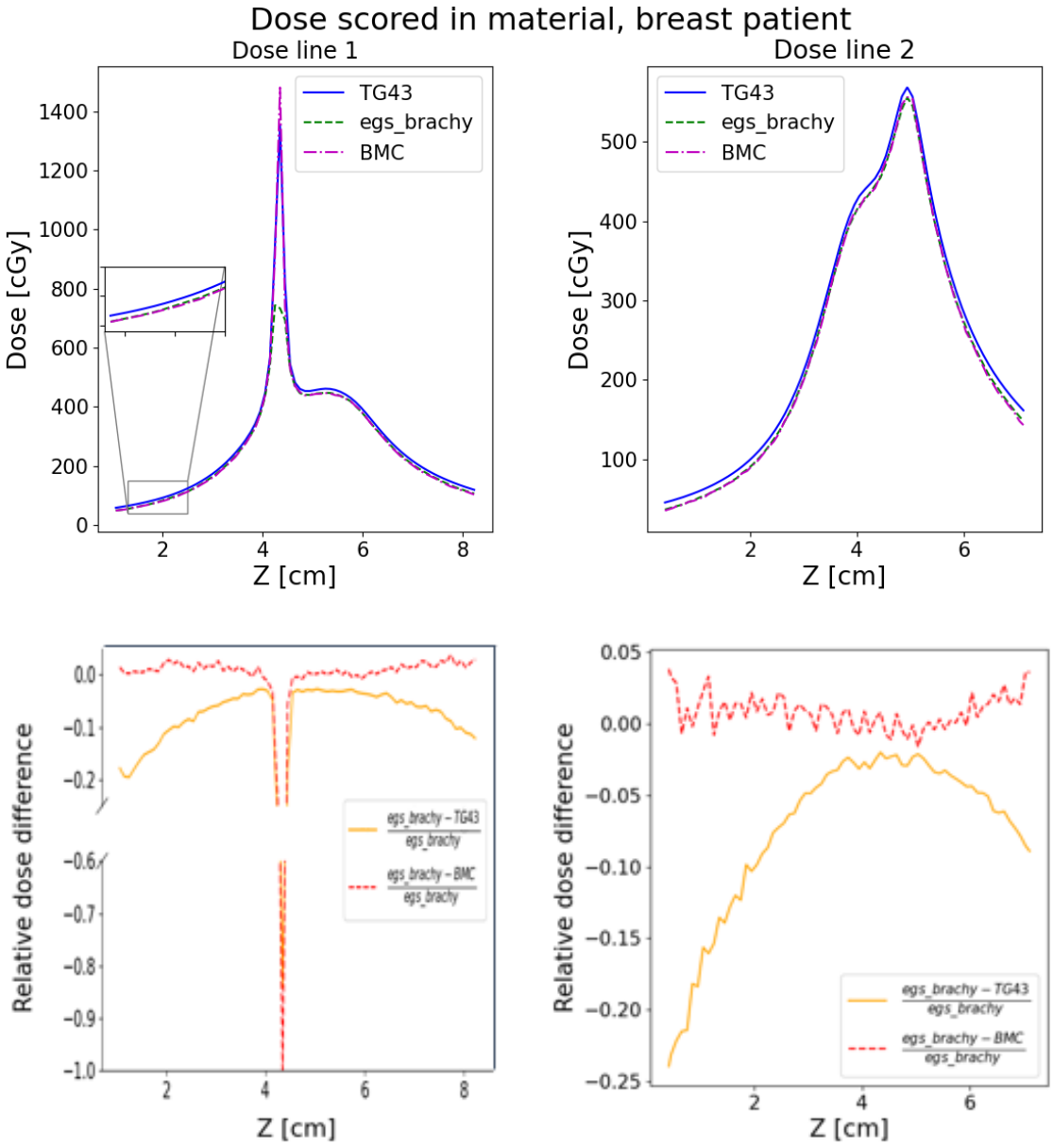

Figure 4.17: Line doses showing the dose scored in material for TG43, egs_brachy and BMC. The bottom part shows the relative dose difference between egs_brachy and the two others. Note that the y-axis for the dose difference in line 1 is broken.

5 | Conclusions

In this study, a characterization of a HDR brachytherapy source and production of a reduced phase space for use in a Monte Carlo dose engine have been performed. Additionally, the study has resulted in simulated dose distributions to be used for comparison of doses calculated by the TG43-formalism and by the brachy Monte Carlo dose engine prototype, that samples particles from the reduced phase space. The analysis of the phase space showed a z dependence in the two angular distributions, but not for the energy. Also a small energy dependence could be found in the two angular distributions, where the particles with lower energies differed from the others. It can be concluded that the direction of the particle is dependent on the other two properties, while the energy can be determined independently. The z position needs to be handled separately due to the two flat surfaces. However, the resulting phase space had a file size small enough to directly be used for sampling and no explicit parameterization of the distributions had to be used at this point. The comparison of dose distributions showed good agreement between the two dose engines and egs_brachy. The limitations of the TG43-formalism could be seen when comparing with dose scored in material for both the head-and-neck case and the breast case. For both material cases, the BMC prototype followed the distribution from egs_brachy well. A larger dose difference could be seen close to dwell positions due to the current dose handling at these locations. A continued development of the BMC will result in new dose distributions that in turn can be compared with the distributions produced in this work. To conclude it all, the reduced phase space has been shown to work as input for the brachy Monte Carlo dose engine prototype and the simulated dose distributions from both patient cases can be utilized in the validation framework for the two dose engines.

5.1 Future work

There are several interesting directions to follow from the outcome of this project. First, the kind of characterization performed should be possible to apply on additional brachytherapy sources with adjustments to the specific geometry. A future goal is to produce a library of phase spaces for the BMC to sample from, for various clinically relevant sources. Something to keep in mind then is that high-energy photon-emitting sources are less sensitive for simulation errors than low-energy sources [12]. A mistake in the geometry design of a low-energy source could therefore result in higher errors in the dose computation.

Secondly, fine tuning of the format of the reduced phase space could be made. The result for the ϕ-distribution showed that the file size could be reduced even more by only storing values of $|\phi|$ and then make a uniform sampling of the sign. The bin size of each parameter in the phase space could also be adaptive instead of fixed. Especially, this could be of interest for the energy where the bin size could be decreased around the peaks and lower energy regions. The continued development of the BMC prototype will also add insights to the analysis of the 4D-histogram and vice versa.

Finally, for the comparison of dose distributions, additional simulations of patient cases as well as single source distributions would yield important information about the performance of the dose engines. Other methods to ensure that the materials used in RayStation and in egs_brachy are identical, could also be of interest.

Bibliography

[1] Socialstyrelsen. (). "Statistik om cancer," [Online]. Available: https://www.socialstyrelsen.se/statistik-och-data/statistik/statistikamnen/cancer/. (accessed: 16.04.2021).

[2] J. Venselaar, A. S. Meigooni, D. Baltas, and P. J. Hoskin, *Comprehensive Brachytherapy: Physical and Clinical Aspects.* Ser. Imaging in medical diagnosis and therapy. CRC Press, 2013, ISBN: 9781138198555.

[3] R. Nath *et al.*, "Dosimetry of interstitial brachytherapy sources: Recommendations of the AAPM Radiation Therapy Committee Task Group No. 43," *Medical Physics*, vol. 22, no. 2, pp. 209–234, 1995. DOI: https://doi.org/10.1118/1.597458. eprint: https://aapm.onlinelibrary.wiley.com/doi/pdf/10.1118/1.597458. [Online]. Available: https://aapm.onlinelibrary.wiley.com/doi/abs/10.1118/1.597458.

[4] M. J. Rivard, B. M. Coursey, L. A. DeWerd, W. F. Hanson, M. Saiful Huq, G. S. Ibbott, M. G. Mitch, R. Nath, and J. F. Williamson, "Update of AAPM Task Group No. 43 Report: A revised AAPM protocol for brachytherapy dose calculations," *Medical Physics*, vol. 31, no. 3, pp. 633–674, 2004. DOI: https://doi.org/10.1118/1.1646040. eprint: https://aapm.onlinelibrary.wiley.com/doi/pdf/10.1118/1.1646040. [Online]. Available: https://aapm.onlinelibrary.wiley.com/doi/abs/10.1118/1.1646040.

[5] S. A. Enger, J. Vijande, and M. J. Rivard, "Model-based dose calculation algorithms for brachytherapy dosimetry," *Seminars in Radiation Oncology*, vol. 30, no. 1, pp. 77–86, 2020, Advances in Brachytherapy, ISSN: 1053-4296. DOI: https://doi.org/10.1016/j.semradonc.2019.08.006. [Online]. Available: https://www.sciencedirect.com/science/article/pii/S1053429619300608.

[6] J. Perez-Calatayud, F. Ballester, R. K. Das, *et al.*, "Dose calculation for photon-emitting brachytherapy sources with average energy higher than 50 kev: Report of the AAPM and ESTRO," *Med Phys*, vol. 39, 5 May 2012. DOI: https://doi.org/10.1118/1.3703892.

[7] K. Abe, N. Kadoya, *et al.*, "Impact of a commercially available model-based dose calculation algorithm on treatment planning of high-dose-rate brachytherapy in patients with cervical cancer," *Journal of Radiation Research*, vol. 59, no. 2, pp. 198–206, Jan. 2018, ISSN: 0449-3060. DOI: 10.1093/jrr/rrx081. eprint: https://academic.oup.com/jrr/article-pdf/59/2/198/26356290/rrx081.pdf. [Online]. Available: https://doi.org/10.1093/jrr/rrx081.

[8] D. Granero, J. Perez-Calatayud, J. Vijande, F. Ballester, and M. J. Rivard, "Limitations of the TG-43 formalism for skin high-dose-rate brachytherapy dose calculations," *Medical Physics*, vol. 41, no. 2, p. 021 703, 2014. DOI: https://doi.org/10.1118/1.4860175. eprint: https://aapm.onlinelibrary.wiley.com/doi/pdf/10.1118/1.4860175. [Online]. Available: https://aapm.onlinelibrary.wiley.com/doi/abs/10.1118/1.4860175.

[9] G. Lymperopoulou, P. Papagiannis, *et al.*, "A dosimetric comparison of and for hdr brachytherapy of the breast, accounting for the effect of finite patient dimensions and tissue inhomogeneities," *Medical Physics*, vol. 33, no. 12, pp. 4583–4589, 2006. DOI: https://doi.org/10.1118/1.2392408. eprint: https://aapm.onlinelibrary.wiley.com/doi/pdf/10.1118/1.2392408. [Online]. Available: https://aapm.onlinelibrary.wiley.com/doi/abs/10.1118/1.2392408.

[10] A. S. Duque, S. Corradini, F. Kamp, *et al.*, "The dosimetric impact of replacing the TG-43 algorithm by model based dose calculation for liver brachytherapy," *Radiat Oncology*, vol. 15, no. 60, 2020. DOI: https://doi.org/10.1186/s13014-020-01492-9.

[11] J. Mikell *et al.*, "U-e-t-425: Impact of Model Based Dose Calculation Algorithm for Ir-192 Intracavitary Brachytherapy with Shielded Applicator," *Medical physics*, vol. 39, pp. 3802–3802, Jun. 2012. DOI: https://doi.org/10.1118/1.4735514.

[12] F. V. Joao Seco, *Monte Carlo Techniques in Radiation Therapy*, ser. Imaging in medical diagnosis and therapy. CRC Press, 2013, ISBN: 978-1-4665-0794-4.

[13] A. Ahnesjö, "Collapsed Cone Convolution of Radiant Energy for Photon Dose Calculation in Heterogeneous Media," *Medical Physics*, vol. 16, no. 4, pp. 577–592, 1989. DOI: https://doi.org/10.1118/1.596360.

[14] J. K. Mikell and F. Mourtada, "Dosimetric impact of an brachytherapy source cable length modeled using a grid-based boltzmann transport equation solver," *Medical Physics*, vol. 37, no. 9, pp. 4733–4743, 2010. DOI: https://doi.org/10.1118/1.3478278. eprint: https://aapm.onlinelibrary.wiley.com/doi/pdf/10.1118/1.3478278. [Online]. Available: https://aapm.onlinelibrary.wiley.com/doi/abs/10.1118/1.3478278.

[15] P. P. Connell and S. Hellman, "Advances in radiotherapy and implications for the next century: A historical perspective," *Cancer Research*, vol. 69, no. 2, pp. 383–392, 2009, ISSN: 0008-5472. DOI: 10.1158/0008-5472.CAN-07-6871. eprint: https://cancerres.aacrjournals.org/content/69/2/383.full.pdf. [Online]. Available: https://cancerres.aacrjournals.org/content/69/2/383.

[16] M. J. Rivard, J. L. M. Venselaar, and L. Beaulieu, "The evolution of brachytherapy treatment planning," *Medical Physics*, vol. 36, no. 6Part1, pp. 2136–2153, 2009. DOI: https://doi.org/10.1118/1.3125136. eprint: https://aapm.onlinelibrary.wiley.com/doi/pdf/10.1118/1.3125136. [Online]. Available: https://aapm.onlinelibrary.wiley.com/doi/abs/10.1118/1.3125136.

[17] Cancerfonden. (). "Strålbehandling - så funkar det," [Online]. Available: https://www.cancerfonden.se/om-cancer/behandlingar/stralbehandling. (Accessed: 02.05.2021).

[18] P. Annede, J.-M. Cosset, E. Van Limbergen, E. Deutsch, C. Haie-Meder, and C. Chargari, "Radiobiology: Foundation and new insights in modeling brachytherapy effects," *Seminars in Radiation Oncology*, vol. 30, no. 1, pp. 4–15, 2020, Advances in Brachytherapy, ISSN: 1053-4296. DOI: https://doi.org/10.1016/j.semradonc.2019.08.009. [Online]. Available: https://www.sciencedirect.com/science/article/pii/S1053429619300633.

[19] J. Skowronek, "Current status of brachytherapy in cancer treatment - short overview," *Journal of contemporary brachytherapy*, vol. 9, no. 6, pp. 581–589, 2017. DOI: https://doi.org/10.5114/jcb.2017.72607.

[20] E. B. Podgorsak, *Review of radiation oncology physics: a handbook for teachers and students*, ser. Educational reports series. International Atomic Energy Agency, Vienna, 2005, ISBN: 92–0–107304–6.

[21] I. Lux and L. Koblinger, *Monte Carlo Particle Transport Methods: Neutron and Photon Calculations*. CRC Press, 1991, ISBN: 0-8493-6074-9.

[22] I. Kawrakow, D. W. O. Rogers, E. Mainegra-Hing, F. Tessier, and B. R. B. Walters, "The EGSnrc code system: Monte Carlo simulation of electron and photon transport," National Research Council Canada, Ottawa, Canada, Tech. Rep. PIRS-701, 2011. [Online]. Available: https://github.com/nrc-cnrc/EGSnrc/raw/gh-pages/doc/pirs701-egsnrc.pdf.

[23] D. Rogers and A. Bielajew, "Monte carlo techniques of electron and photon transport for radiation dosimetry," *The dosimetry of ionizing radiation*, vol. 3, pp. 427–539, Jan. 1990.

[24] J. M. Hammersley and D. C. Handscomb, *Monte Carlo Methods*. Springer, Dordrecht, 1964, ISBN: 978-94-009-5821-0. DOI: https://doi.org/10.1007/978-94-009-5819-7.

[25] D. W. O. Rogers, "Fifty years of Monte Carlo simulations for medical physics," *Physics in Medicine and Biology*, vol. 51, no. 13, R287–R301, Jun. 2006. DOI: 10.1088/0031-9155/51/13/r17. [Online]. Available: https://doi.org/10.1088/0031-9155/51/13/r17.

[26] D. W. O. Rogers, B. Walters, and I. Kawrakow, "BEAMnrc Users Manual," Tech. Rep., 2005.

[27] B. Walters and I. Kawrakow, "DOSXYZnrc Users Manual," 2016.

[28] M. J. P. Chamberland, R. E. P. Taylor, D. W. O. Rogers, and R. M. Thomson, "egs_brachy: A versatile and fast Monte Carlo code for brachytherapy," *Phys. Med. Bio.*, vol. 61, no. 23, pp. 8214–8231, 2016.

[29] M. Berger and J. Hubbell, "Xcom: Photon cross sections on a personal computer," Jul. 1987. DOI: 10.2172/6016002. [Online]. Available: https://www.osti.gov/biblio/6016002.

[30] G. Daskalov *et al.*, "Monte carlo-aided dosimetry of a new high dose-rate brachytherapy source," *Medical physics*, vol. 25, no. 11, pp. 2200–2208, 1998. DOI: https://doi.org/10.1118/1.598418.

[31] R. Capote *et al.*, "Summary Report of a Consultants Meeting on Phase-Space Database for External Beam Radiotherapy, Vienna, 12-14 December 2005," International Atomic Energy Agency, Vienna, Austria, Jan. 2006.

[32] R. M. Thomson, R. E. P. Taylor, M. J. P. Chamberland, and D. W. O. Rogers, "User manual for egs_brachy. a versatile and fast EGSnrc application for brachytherapy," Carleton Laboratory for Radiotherapy Physics, Tech. Rep. Report CLRP-17-02.

[33] RayStation, *RayStation 10B reference manual*, 2021.

[34] D. A. Low, W. B. Harms, S. Mutic, and J. A. Purdy, "A technique for the quantitative evaluation of dose distributions," *Medical physics*, vol. 25, no. 5, pp. 656–661, 1998. DOI: https://doi.org/10.1118/1.598248.

DEPARTMENT OF MATHEMATICAL SCIENCES
CHALMERS UNIVERSITY OF TECHNOLOGY
Gothenburg, Sweden
www.chalmers.se

CHALMERS
UNIVERSITY OF TECHNOLOGY